

Scalable production of uniform and mature organoids in a 3D geometrically-engineered permeable membrane

Received: 18 December 2023

Accepted: 30 September 2024

Published online: 31 October 2024

 Check for updates

Dohui Kim^{1,6}, Hyeonji Lim^{2,6}, Jaeseung Youn¹, Tae-Eun Park^{2,7}   & Dong Sung Kim^{1,3,4,5,7}  

The application of organoids has been limited by the lack of methods for producing uniformly mature organoids at scale. This study introduces an organoid culture platform, called UniMat, which addresses the challenges of uniformity and maturity simultaneously. UniMat is designed to not only ensure consistent organoid growth but also facilitate an unrestricted supply of soluble factors by a 3D geometrically-engineered, permeable membrane-based platform. Using UniMat, we demonstrate the scalable generation of kidney organoids with enhanced uniformity in both structure and function compared to conventional methods. Notably, kidney organoids within UniMat show improved maturation, showing increased expression of nephron transcripts, more in vivo-like cell-type balance, enhanced vascularization, and better long-term stability. Moreover, UniMat's design offers a more standardized organoid model for disease modeling and drug testing, as demonstrated by polycystic-kidney disease and acute kidney injury modeling. In essence, UniMat presents a valuable platform for organoid technology, with potential applications in organ development, disease modeling, and drug screening.

Organoids, which self-organize into complex multicellular structures from human stem cells, have the potential to recapitulate the structural and functional units of their corresponding organs in the human body^{1,2}. As a result, organoids have emerged as promising in vitro tools for investigating human organogenesis and disease, as well as for screening therapeutic molecules^{3,4}. Despite significant progress in generating organoids that possess a complexity akin to in vivo physiological systems, their widespread adoption in clinical trial validation and pharmaceutical drug development remains limited. This limitation is primarily attributed to the high variability observed in organoid morphology, function, and formation efficiency⁵. Such variability is especially prevalent in organoids formed without physical

constraints⁶. For example, organoids generated through spontaneous self-organization within extracellular matrix (ECM) hydrogels, such as Matrigel or Geltrex^{7,8}, frequently exhibit considerable variations in size, shape, and differentiation⁶. This phenomenon stems from the inherently non-linear and deterministic nature of organogenesis and organoid formation, where even slight deviations in initial condition can lead to significant differences in the final morphogenesis⁹. This inconsistency complicates accurate experimental comparisons and compromises the reliability of outcomes, thereby posing challenges to the standardization of organoid-based assays¹⁰.

To address these issues, researchers have employed microwell platforms. These are engineered polymeric substrates designed with

¹Department of Mechanical Engineering, Pohang University of Science and Technology (POSTECH), Pohang, South Korea. ²Department of Biomedical Engineering, College of Information and Biotechnology, Ulsan National Institute of Science and Technology (UNIST), Ulsan, South Korea. ³Department of Chemical Engineering, Pohang University of Science and Technology (POSTECH), Pohang, South Korea. ⁴School of Interdisciplinary Bioscience and Bioengineering, Pohang University of Science and Technology (POSTECH), Pohang, South Korea. ⁵Institute for Convergence Research and Education in Advanced Technology, Yonsei University, Seoul, South Korea. ⁶These authors contributed equally: Dohui Kim, Hyeonji Lim. ⁷These authors jointly supervised this work: Dong Sung Kim, Tae-Eun Park.  e-mail: tepark@unist.ac.kr; smkds@postech.ac.kr

microcavities that serve as physical constraints in organoid culture. Microwells offer a solution to reduce variability in organoid development by controlling cellular density and the geometry of either embryonic bodies^{11–13} or aggregates of differentiated progenitor cells^{8,14,15}, thereby allowing for precise guidance over the initial geometry of organoids. Furthermore, microwell platforms designed with a microwell array facilitate the formation of an array of organoids, thus improving the scalability essential for high-throughput organoid assays. Recently, various organoids, including those resembling the pancreas¹¹, intestinal¹⁴, lung¹², and kidney¹⁵, have been successfully generated using microwell platforms, exhibiting improved uniformity. Nonetheless, conventional microwell platforms have significant limitations. Their small dimensions and confined spaces of impermeable microwells can obstruct the efficient diffusion of soluble factors from the surrounding medium to the organoids. This can lead to an accumulation of metabolic wastes around the organoids and a restricted supply of nutrients, growth factors, and oxygen vital for organoid growth and maturation^{16–18}. As organoids grow, their need for nutrients, growth factors, and oxygen escalates, potentially exceeding the diffusion capacities of impermeable microwells. While previous studies have proposed integrating bioreactors, such as microfluidic chips, with microwells to enhance the diffusion of soluble factors via a continuous medium flow^{19–21}, implementing such a solution is not straightforward. This complexity limits the widespread use of these methods.

Here, we propose a versatile organoid culture platform designed to address current challenges, facilitating the scalable generation of organoids that are not only uniform but also mature. Our approach encompasses the development of 3D geometrically-engineered, permeable membranes that provide geometrical constraints, yet allow for the unhindered exchange of soluble factors. By incorporating this 3D permeable membrane into a cell culture insert, our platform seamlessly adapts to standard cell culture plates, obviating the need for alterations to established protocols or workflows. Employing this platform for the scalable production of human induced pluripotent stem cell (hiPSC)-derived kidney organoids, we have demonstrated the effectiveness of our method. It not only improves the uniformity and maturity of kidney organoids but also exhibits enhanced performance in organoid-based disease modeling and drug testing. This underscores the potential of our 3D geometrically-engineered, permeable membrane as a benchmark tool for organoid-based assays.

Results

Design and fabrication of 3D geometrically-engineered, permeable membrane for organoid culture platform

To generate organoids that are not only uniform but also mature at a scalable level, we first aimed to establish an organoid culture platform. This platform offers both geometrical constraints for precise organoid regulation and an unrestricted supply of soluble factors, ensuring the efficient diffusion and exchange of nutrients, growth factors, and oxygen (Fig. 1a). We named this platform UniMat (Uniform and Mature organoid culture platform), and developed it based on three primary design criteria:

(1) UniMat should efficiently partition individual organoids, providing geometrical constraints that ensure organoid uniformity;

(2) The individual microwells in UniMat should promote cell aggregation, which is essential for the initial formation of cohesive 3D aggregates crucial to organoid development;

(3) UniMat should possess a porous structure, creating a permeable environment that facilitates an unrestricted supply of soluble factors necessary for organoid maturation.

To realize this concept, we engineered a flat nanofiber (NF) membrane into a 3D permeable microwell array, maintaining a porous membrane structure to ensure high permeability to both gases and solutes.

To fabricate the UniMat, we employed the electrospinning process, followed by a subsequent matched-mold thermoforming process, based on our previous work²² (Fig. 1b). In this study, we developed a NF membrane composed of polycaprolactone (PCL) and Pluronic F108 (PF108) NFs. The selection of PCL was based on its wide use in electrospinning and excellent biocompatibility^{23,24}. PF108, an amphiphilic synthetic polymer, was incorporated to increase the hydrophilicity of the membrane^{25,26} (Supplementary Fig. 1a). This hydrophilic membrane reduced light scattering in a liquid cell culture medium by minimizing differences in refractive indices between the NF membrane and the surrounding medium, thus enhancing light transmittance (Supplementary Fig. 1b), which improves cell observation²⁷. The manufactured NF membranes exhibited consistent physical properties, including membrane thickness and NF diameter distribution, across different experimental batches under our defined conditions (Supplementary Figs. 1c, d), paving the way for the standardized production of reliable and uniform UniMat. The matched-mold thermoforming process allowed for precise microstructuring of a thin and flat NF membrane, ranging in thickness from 50 μm to 150 μm , into a 3D shape. This results in improved shape flexibility and replication fidelity without compromising the porous structure of the NF membrane. Leveraging this capability, we successfully engineered an electrospun free-standing NF membrane with a thickness of 50 μm into a 3D microwell array-structured membrane, resulting in a UniMat. Subsequently, the UniMat was incorporated into the bottom opening of a custom-made 24-well insert wall in a free-standing configuration, allowing for compatibility with standard cell culture plates (Fig. 1c). The successful fabrication of UniMat, with its 3D microwell array-structured NF membrane, was confirmed using scanning electron microscopy (SEM) analysis (Fig. 1d).

In this study, we fabricated the UniMat by microstructuring an electrospun NF membrane to form a V-shaped microwell array (Fig. 1e), promoting the collection and aggregation of seeded cells at the bottom regions of microwells. The V-shaped design enhances cell confinement owing to its inclined walls, ensuring a more defined region for cell placement within every microwell. Importantly, by merely modifying the mold geometry used in the matched-mold thermoforming process, the size of the microwells could be tuned to accommodate the growth of organoids of various sizes. We fabricated three different types of UniMats, each with distinct width and depth dimensions: UniMat400 (width: 400 μm , depth: 343 μm), UniMat600 (width: 600 μm , depth: 517 μm), and UniMat800 (width: 800 μm , depth: 691 μm) (Supplementary Fig. 2). The microwell in the UniMat preserved a porous architecture similar to the original NF membrane (Fig. 1f), and possessed a thin wall thickness of approximately 30 μm (Fig. 1g). These characteristics enabled the UniMat to display a high permeability for molecules of varying molecular weights, which was more than twice that of a conventional PET porous membrane (Fig. 1h).

To validate the capability of the UniMat to generate uniform and mature organoids, we selected kidney organoids as a representative lineage of organs. Kidney organoids are complex and hold significant biomedical interest because of their potential applications in disease modeling and drug testing. For the differentiation of kidney organoids, we optimized the Morizane protocol²⁸, to ensure the consistent generation of kidney organoids from human induced pluripotent stem cells (hiPSCs) in 3D culture platforms (Supplementary Notes 1 and 2 and Supplementary Figs. 3 and 4). This refined protocol was then seamlessly incorporated into the UniMat, where nephron progenitor cells (NPCs) derived from hiPSCs were seeded onto the UniMat400, which was coated with a thin layer of agarose hydrogel to enhance low attachment condition at the bottom of UniMat, on day 9. The subsequent differentiation processes within the UniMat400 led to the formation of kidney organoids by day 24–26 (Fig. 1i). Notably, the sharp angle and narrow base of the NF microwell guided cells towards the

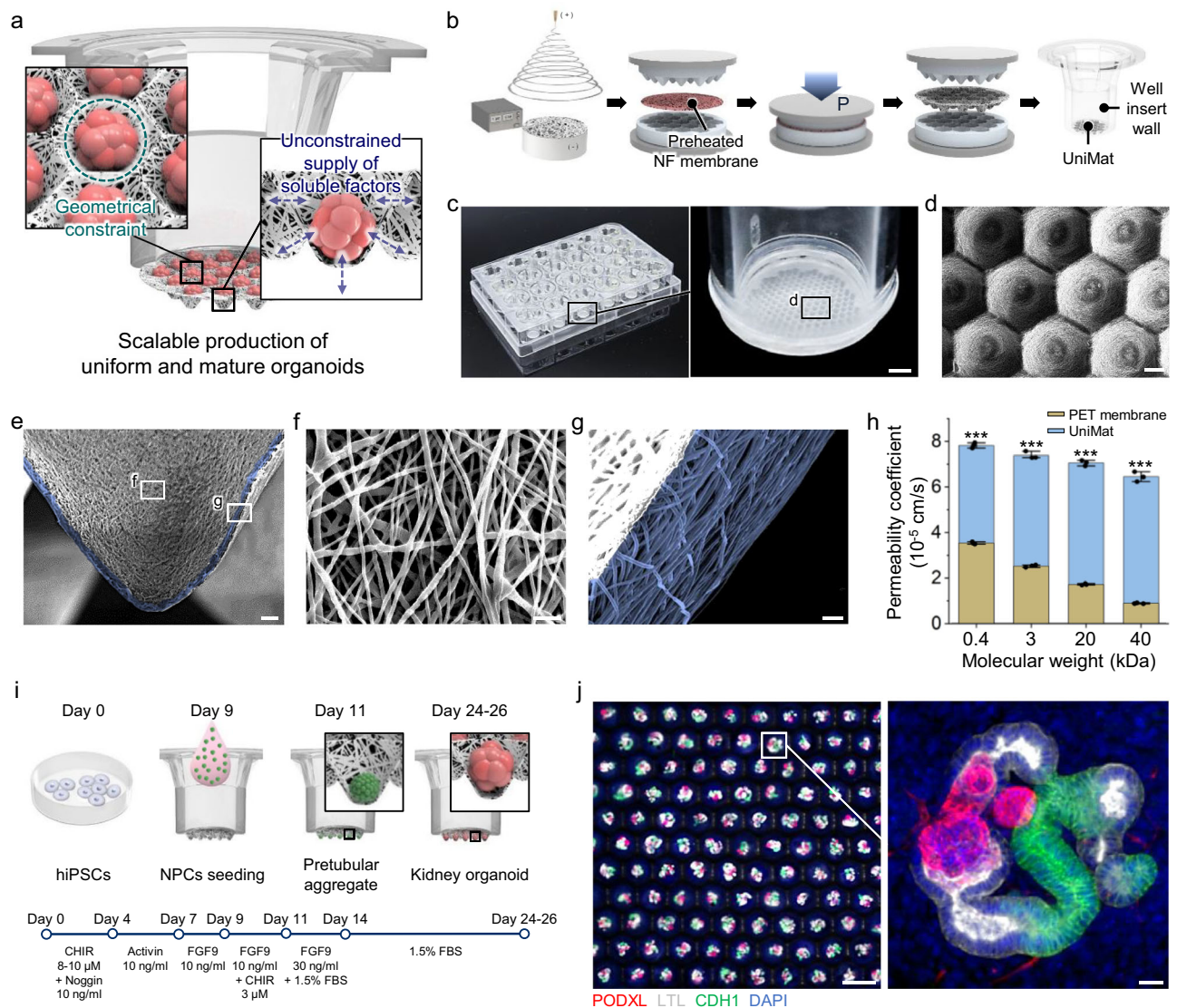


Fig. 1 | Development of UniMat for uniform and mature organoid culture.

a Schematic of UniMat, which simultaneously provides geometrical constraints and unconstrained supply of soluble factors, integrated into bottom opening of well insert. **b** Illustration of fabrication of UniMat using a matched-mold thermoforming process with electrospun nanofiber (NF) membrane. **c** Photographs of UniMat-incorporated well inserts placed in standard 24-well cell culture plate. Scale bar = 1 mm. **d** Top SEM image of UniMat consisting of 3D microwell array-structured NF membrane. Scale bar = 100 μ m. **e** Cross-sectional SEM image of V-shaped single microwell in UniMat. Scale bar = 25 μ m. Three independent experiments were conducted to produce three different samples, and imaging was independently repeated with similar results. **f** Magnified SEM image of microwell surface in UniMat showing porous structure of NF membrane. Scale bar = 2 μ m. Three independent experiments were conducted to produce three different samples, and imaging was

independently repeated with similar results. **g** Magnified SEM image of a nanofibrous wall of V-shaped microwell. Scale bar = 5 μ m. Three independent experiments were conducted to produce three different samples, and imaging was independently repeated with similar results. **h** Permeability coefficients across UniMat and PET membrane ($n = 3$ samples, mean \pm SD). Significance by Student's *t*-test: $P = 5.2 \times 10^{-7}$ (0.4 kDa); $P = 9.5 \times 10^{-7}$ (3 kDa); $P = 2.1 \times 10^{-7}$ (20 kDa); $P = 9.1 \times 10^{-11}$ (40 kDa). **i** Schematic of optimized protocol for generation of kidney organoids from hiPSCs in UniMat. **j** Confocal z-stack images of kidney organoids cultured in UniMat, stained with PODXL, LTL, and CDH1. Scale bars = 400 μ m (left) and 20 μ m (right). Four independent experiments were conducted, and imaging was independently repeated with similar results. Source data are provided as a Source Data file.

center of each microwell, thereby enhancing cell-to-cell contact and promoting aggregate formation. This strategic approach successfully addressed the challenges encountered with the previously utilized U-shaped configuration²², where evenly distributed NPCs along the U-well curve resulted in low aggregation efficiency, thus restricting the ability to achieve stable and consistent aggregates crucial for reliably producing uniform organoids (Supplementary Fig. 5). Upon differentiation, the majority of kidney organoids exhibited nephron-like structures, including podocytes (PODXL⁺), proximal tubules (LTL⁺), and distal tubules (CDH1⁺), within the UniMat (Fig. 1j). As a result, approximately 87 \pm 5% of all pretubular aggregates were successfully

developed into nephron-like kidney organoids, achieving around 5 organoids per mm² within the UniMat400.

UniMat improves uniformity of organoids

Having demonstrated the successful production of kidney organoids in the UniMat400, we utilized it as a model to explore its potential to reduce the variability of organoids. We assessed the morphological consistency in size and structure of kidney organoids in the UniMat platforms (Fig. 2a), which provide geometric guidance from the NPC stage. This was further compared to the uniformity observed in organoids that were exclusively generated on a plate coated with

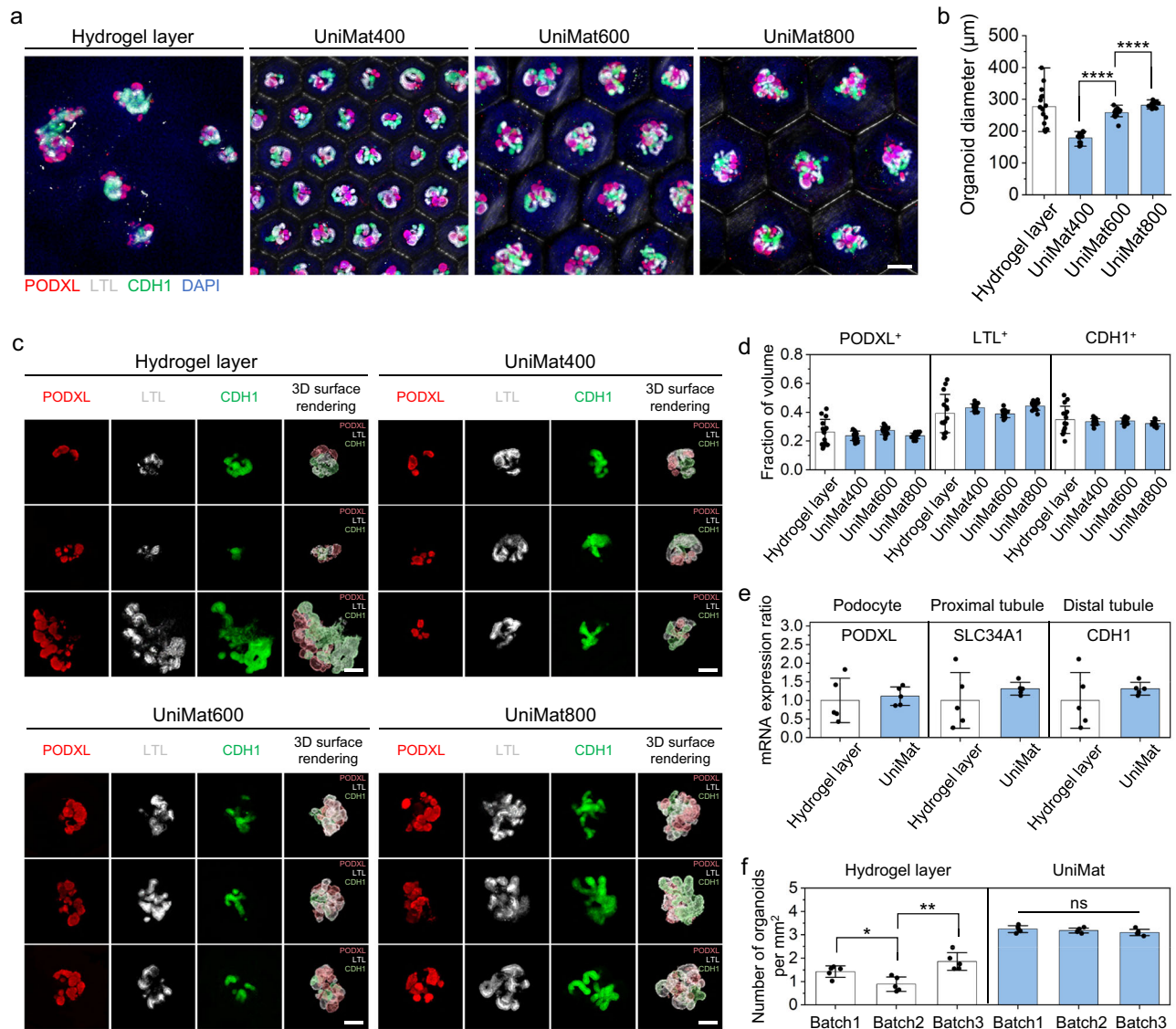


Fig. 2 | Generation of uniform kidney organoids in UniMat. **a** Confocal z-stack images of kidney organoids cultured in hydrogel layer (Geltrex), UniMat400, UniMat600, and UniMat800, stained with PODXL, LTL, and CDH1. Scale bar = 200 μm . **b** Measured diameters of kidney organoids formed in hydrogel layer, UniMat400, UniMat600, and UniMat800 ($n = 15$ organoids, mean \pm SD). Significance by one-way ANOVA with Tukey's multiple comparisons test: $P_{\text{UniMat400}}$, $P_{\text{UniMat600}} = 1.3 \times 10^{-11}$, $P_{\text{UniMat800}} = 8.5 \times 10^{-5}$. **c** Confocal z-stack images for markers of podocytes (PODXL), proximal tubules (LTL), and distal tubules (CDH1), and corresponding Imaris 3D surface rendering images of kidney organoids cultured in hydrogel layer, UniMat400, UniMat600, and UniMat800. Scale bars = 100 μm . **d** Quantitative analysis of PODXL⁺ podocytes, LTL⁺ proximal tubules,

and CDH1⁺ distal tubules fractions with respect to total volume in individual kidney organoids generated in hydrogel layer, UniMat400, UniMat600, and UniMat800 ($n = 15$ organoids, mean \pm SD). Significance by one-way ANOVA with Tukey's multiple comparisons test. **e** qRT-PCR of PODXL, SLC34A1, and CDH1 expressions of kidney organoids cultured in hydrogel layer and UniMat ($n = 5$ independent experiments, mean \pm SD). **f** Organoid formation efficiency of kidney organoids in hydrogel layer and UniMat cultured from three independent batches of differentiation ($n = 5$ samples, mean \pm SD). Significance by one-way ANOVA with Tukey's multiple comparisons test: $P_{\text{batch1, batch2}} = 0.0161$, $P_{\text{batch2, batch3}} = 0.0022$ (hydrogel layer). Source data are provided as a Source Data file.

Geltrex hydrogel (hereinafter referred to as the hydrogel layer), without any physical constraints (Fig. 2a). Notably, kidney organoids cultured in each UniMat demonstrated a more consistent size distribution compared to those on the hydrogel layer (Fig. 2b and Supplementary Table 1). Moreover, the size of organoids, including diameter and height, appeared to be regulated through the UniMat-based culture, correlating with the size of the V-shaped microwells in the UniMat (Fig. 2b and Supplementary Fig. 6).

To delve deeper into the mechanism by which UniMat controls the organoid size, we examined the initial aggregate size, which is known to influence organogenesis and organoid formation. Given the distinct sizes and arrays of V-shaped microwells in each of the UniMat400, UniMat600, and UniMat800 (Supplementary Fig. 7a), we

noted that within 6 h of seeding, aggregates were formed in sizes corresponding to each specific UniMat (Supplementary Fig. 7b). These measured sizes closely matched with the estimated sizes based on the geometrical data of the microwells and the average number of cell sedimentations per microwell in each UniMat (Supplementary Note 3 and Supplementary Fig. 7c-f). Our findings suggest that by adjusting both the microwell size and the cell seeding density in the UniMat, the initial aggregate size can be effectively modulated. Notably, the size variances among the organoids grown in different UniMats were consistent with the trends observed in the initial aggregate sizes, underscoring the pivotal role of UniMat in determining organoid size.

Having established that the UniMat can effectively regulate organoid size, we further investigated the structural variability of

kidney organoids. Using confocal imaging rendered with the Imaris 3D surface rendering software, we quantified the presence of glomerular podocytes (PODXL⁺), proximal tubules (LTL⁺), and distal tubules (CDH1⁺) in individual kidney organoids (Fig. 2c). Subsequently, we evaluated the distribution of these key structures by calculating the fraction of each structure's volume relative to the total volume of each organoid. Notably, while the average fractions of each structure were comparable between organoids cultured on the hydrogel layer and those in the UniMat, kidney organoids cultured in the UniMat exhibited less structural variability compared to those cultured on the hydrogel layer (Fig. 2d and Supplementary Table 2). These findings indicate that the geometrical constraints provided by the UniMat promote the production of organoids with more uniform sizes and structures. Especially in the UniMat800, we observed a greater reduction in structural variability, with a 4-fold decrease in podocytes, a 5-fold decrease in proximal tubules, and a 4-fold decrease in distal tubules, as compared to the organoids cultured on the hydrogel layer (Supplementary Table 2). Based on our data, the UniMat800-cultured kidney organoids exhibited greater uniformity and they had an average size comparable to those cultured on the hydrogel layer. In this regard, UniMat800 was selected as the representative UniMat for further experiments.

To further assess the potential of UniMat in improving the functional uniformity of organoids, we randomly selected 10 organoids from both the hydrogel layer and UniMat. We then performed a quantitative real-time polymerase chain reaction (qRT-PCR) analysis to quantify the expression levels of key genes associated with podocytes (PODXL), proximal tubules (SLC34A1), and distal tubules (CDH1). Intriguingly, in accordance with the reduced structural variability observed in UniMat, the organoids cultured in UniMat exhibited less gene expression heterogeneity compared to those grown on the hydrogel layer (Fig. 2e and Supplementary Table 3). These results underscore the UniMat's ability to enhance functional uniformity in organoids, demonstrating its potential to yield more precise and consistent experimental results. Moreover, UniMat showed a capacity to improve the uniformity of organoid formation efficiency, which is quantified as the number of organoids formed per mm². In determining this efficiency, the variability in the UniMat-based culture was substantially lower than in the hydrogel layer-based culture (Fig. 2f and Supplementary Table 4). Notably, the formation efficiency was relatively consistent across three independent batches for the UniMat-based cultures (Fig. 2f and Supplementary Table 4). These findings highlight the reproducibility of organoid formation through the UniMat, suggesting that the UniMat provides a consistent and reliable platform for generating uniform organoids in a scalable manner.

UniMat enhances maturity of organoids

After examining organoid uniformity, we investigated if the utilization of the permeable UniMat could promote the maturation of organoids, thereby addressing the limitations associated with conventional impermeable microwell platforms. For this experiment, we employed the AggreWell™800 Microwell Plate (hereinafter referred to as AggreWell), as a representative conventional microwell platform, with a width of 800 μm, similar to the dimensions of the UniMat used in this study. Confocal microscopic analysis revealed the formation of kidney organoids with nephron-like structures, including glomerular podocytes (PODXL⁺), proximal tubules (LTL⁺), and distal tubules (CDH1⁺), in both the AggreWell and UniMat (Fig. 3a and Supplementary Fig. 8a). However structural distribution differed between the two platforms. Specifically, the UniMat-cultured organoids had fewer podocytes but more proximal and distal tubule structures compared to AggreWell-cultured organoids (Fig. 3b). Despite the lower podocyte distribution in UniMat, these podocytes in the UniMat displayed mature characteristics with the basally localized expression of ZO-1 at the edge of cell-cell joints (Fig. 3c), which is a marker associated with tight junction

observed within podocyte slit diaphragms in the native kidney tissue²⁹ and mature kidney organoids³⁰. qRT-PCR analysis also highlighted the upregulated expressions of NPHS1 and PODXL (Supplementary Fig. 8b), both essential for podocyte integrity and function, serving as markers for the slit diaphragm in glomerular filtration^{31,32}. This suggests that our UniMat can generate mature kidney organoids with mature glomerular cells, a contrast to those produced by the AggreWell-based culture. Furthermore, the kidney organoids cultured in UniMat exhibited morphogenesis of tubular structures, as evidenced by polarized proximal tubules with apical enrichment of the brush border marker LTL³³ (Fig. 3d). Consistent with this polarization, there was an upregulation of mRNA expression levels for ABCB1, AQP1, and SLC34A1, which are vital for the proximal tubule's functions in solute transport and water reabsorption, essential components of the kidney's filtration and absorption systems^{34–36}. Furthermore, UMOD, which plays a crucial role in urine concentration within the loop of Henle^{37,38}, and CDH1, reflecting epithelial integrity within the distal tubules³⁹, also showed increased expression levels in the kidney organoids cultured in the UniMat (Supplementary Fig. 8c). This indicates enhanced functional potential compared to the kidney organoids cultured in the AggreWell. To further examine the physiological relevance of the tubular functions of these kidney organoids, we performed an *in vitro* dextran uptake assay. After a 24-h exposure to 10 kDa dextran, selective uptake of dextran within LTL⁺ proximal tubules confirmed the absorptive functionality of the UniMat-cultured kidney organoids (Fig. 3e). Specifically, these kidney organoids demonstrated the ability to uptake and retain dextran within LTL⁺ proximal tubule epithelial cells (Fig. 3e), indicating their capacity for reabsorption.

Having identified that kidney organoids formed in the permeable UniMat exhibited greater maturity than those in the impermeable microwells, we next addressed the question of how the unconstrained supply of soluble factors through the 3D geometrically-engineered, permeable membrane in the UniMat influences the maturity of organoids. This question also arose in light of the limitation of conventional impermeable microwell platforms. We initially investigated whether the enhanced maturation of kidney organoids in UniMat was due to its permeable environment affecting the survival of NPCs. Viability tests on day 11 showed no significant difference in NPC survival rates between the UniMat and AggreWell (Supplementary Fig. 9). This led us to conclude that the mature kidney organoids in UniMat result from the facilitated supply of soluble factors during NPC differentiation, rather than differences in survival of NPC aggregates. To further explore the impact of UniMat's permeability on organoid maturity, we fabricated two different UniMat variants with distinct permeability characteristics. We achieved these characteristics by strategically blocking the pores of the NF membrane through precise adjustments of the matched-mold thermoforming process conditions (Fig. 3f). One variant, named UniMat-LP, was designed to have a lower permeability than the original UniMat, resembling the permeability of a conventional PET membrane (Fig. 3g). The second variant, UniMat-ZP, exhibited zero permeability (Fig. 3g). These modifications allowed for controlled studies on the influence of different levels of UniMat permeability on organoid maturation. Our spatiotemporal numerical simulations predicted active glucose diffusion around a single kidney organoid situated in a microwell of the original UniMat, supplied from the culture medium through its permeable nanofibrous wall within 72 h (Fig. 3h). However, with the reduced permeability, the glucose diffusion level around the kidney organoid decreased, as observed in both UniMat-LP and UniMat-ZP (Fig. 3h). This glucose diffusion simulation highlighted the effectiveness of UniMat's permeability in facilitating nutrient supply to organoids. Notably, in concordance with the simulation results, mRNA expression levels of NPHS1, PODXL (podocyte), ABCB1, AQP1, SLC34A1 (proximal tubule), UMOD (loop of Henle), and CDH1 (distal tubule) increased in response to the

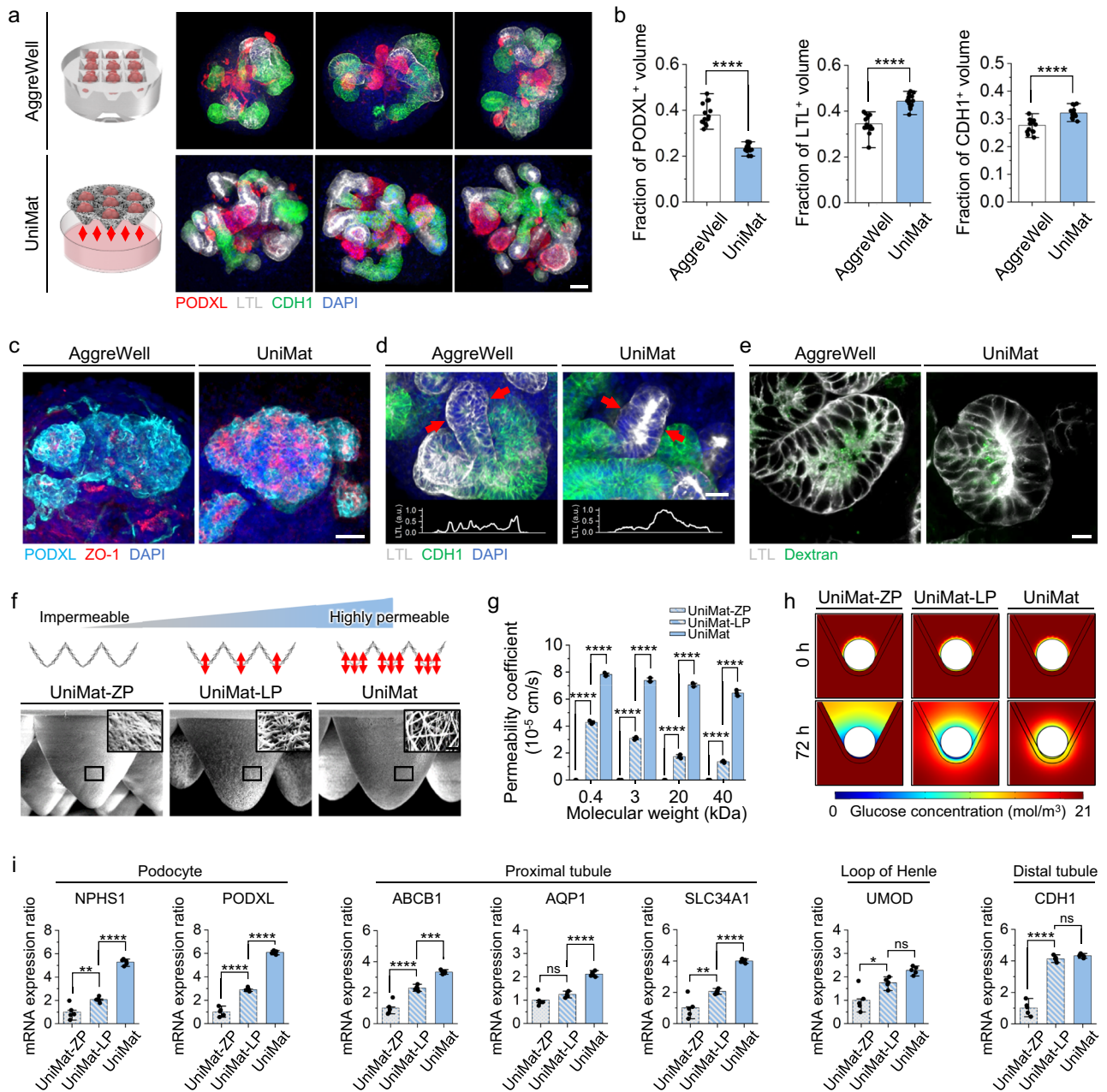


Fig. 3 | Generation of mature kidney organoids in UniMat. **a** Confocal images of kidney organoids in AggreWell and UniMat, stained with PODXL, LTL, and CDH1. Scale bar = 50 μm . **b** Quantification of PODXL⁺, LTL⁺, and CDH1⁺ fractions in individual organoids in AggreWell and UniMat ($n = 15$ organoids, mean \pm SD). Significance by one-way ANOVA with Tukey's multiple comparisons test: $P = 3.3 \times 10^{-11}$ (PODXL⁺); $P = 2.4 \times 10^{-8}$ (LTL⁺); $P = 1.2 \times 10^{-5}$ (CDH1⁺). **c** Immunofluorescence images of PODXL and ZO-1 of kidney organoids in AggreWell and UniMat. Scale bar = 20 μm . **d** Immunofluorescence images of LTL of kidney organoids in AggreWell and UniMat. Scale bar = 20 μm . Bottom plots show LTL intensity across line scans marked by red arrows in the images above. **e** Dextran uptake assay in LTL⁺ proximal tubules of kidney organoids in AggreWell and UniMat. Scale bar = 10 μm . **f** SEM images of microwell in UniMat-ZP, UniMat-LP, and original UniMat with magnified SEM images of microwell walls. Scale bar = 100 μm and 2 μm (Inset images). **g** Permeability coefficients across UniMat-ZP, UniMat-LP, and UniMat ($n = 3$ samples, mean \pm SD). Significance by one-way ANOVA with Tukey's multiple comparisons test: $P_{\text{UniMat-ZP, UniMat-LP}} = 7.5 \times 10^{-10}$, $P_{\text{UniMat-LP, UniMat}} = 1.1 \times 10^{-8}$ (0.4 kDa); $P_{\text{UniMat-ZP, UniMat-LP}} = 1.4 \times 10^{-7}$, $P_{\text{UniMat-LP, UniMat}} = 4.8 \times 10^{-9}$ (3 kDa); $P_{\text{UniMat-ZP, UniMat-LP}} = 2.2 \times 10^{-6}$, $P_{\text{UniMat-LP, UniMat}} = 9.1 \times 10^{-11}$ (20 kDa); $P_{\text{UniMat-ZP, UniMat-LP}} = 3.6 \times 10^{-5}$, $P_{\text{UniMat-LP, UniMat}} = 7.8 \times 10^{-9}$ (40 kDa). **h** Numerical simulations of glucose concentration distribution around organoid in UniMat-ZP, UniMat-LP, and UniMat. **i** qRT-PCR of kidney organoids in UniMat-ZP, UniMat-LP, and UniMat ($n = 5$ independent experiments, mean \pm SD). Significance by one-way ANOVA with Tukey's multiple comparisons test: $P_{\text{UniMat-ZP, UniMat-LP}} = 0.0037$, $P_{\text{UniMat-LP, UniMat}} = 8.2 \times 10^{-8}$ (NPHS1); $P_{\text{UniMat-ZP, UniMat-LP}} = 1.0 \times 10^{-7}$, $P_{\text{UniMat-LP, UniMat}} = 3.1 \times 10^{-10}$ (PODXL); $P_{\text{UniMat-ZP, UniMat-LP}} = 1.9 \times 10^{-5}$, $P_{\text{UniMat-LP, UniMat}} = 0.0002$ (ABCB1); $P_{\text{UniMat-LP, UniMat}} = 1.6 \times 10^{-5}$ (AQP1); $P_{\text{UniMat-ZP, UniMat-LP}} = 0.0031$, $P_{\text{UniMat-LP, UniMat}} = 1.4 \times 10^{-5}$ (SLC34A1); $P_{\text{UniMat-ZP, UniMat-LP}} = 0.0104$, (UMOD); $P_{\text{UniMat-ZP, UniMat-LP}} = 2.2 \times 10^{-9}$ (CDH1). Source data are provided as a Source Data file.

enhanced permeability (Fig. 3i). Therefore, our findings indicated that the unconstrained supply of soluble factors within the UniMat, facilitated by high permeability through the 3D geometrically-engineered, permeable membrane, enables the generation of mature kidney organoids.

UniMat enhances vascularization of organoids

Engineering vascularization of organoids stands as one of the primary objectives in ongoing research efforts to advance organoid technology⁴⁰. In kidney development, vascularization plays a crucial role and is closely linked to the maturation of other cell types.

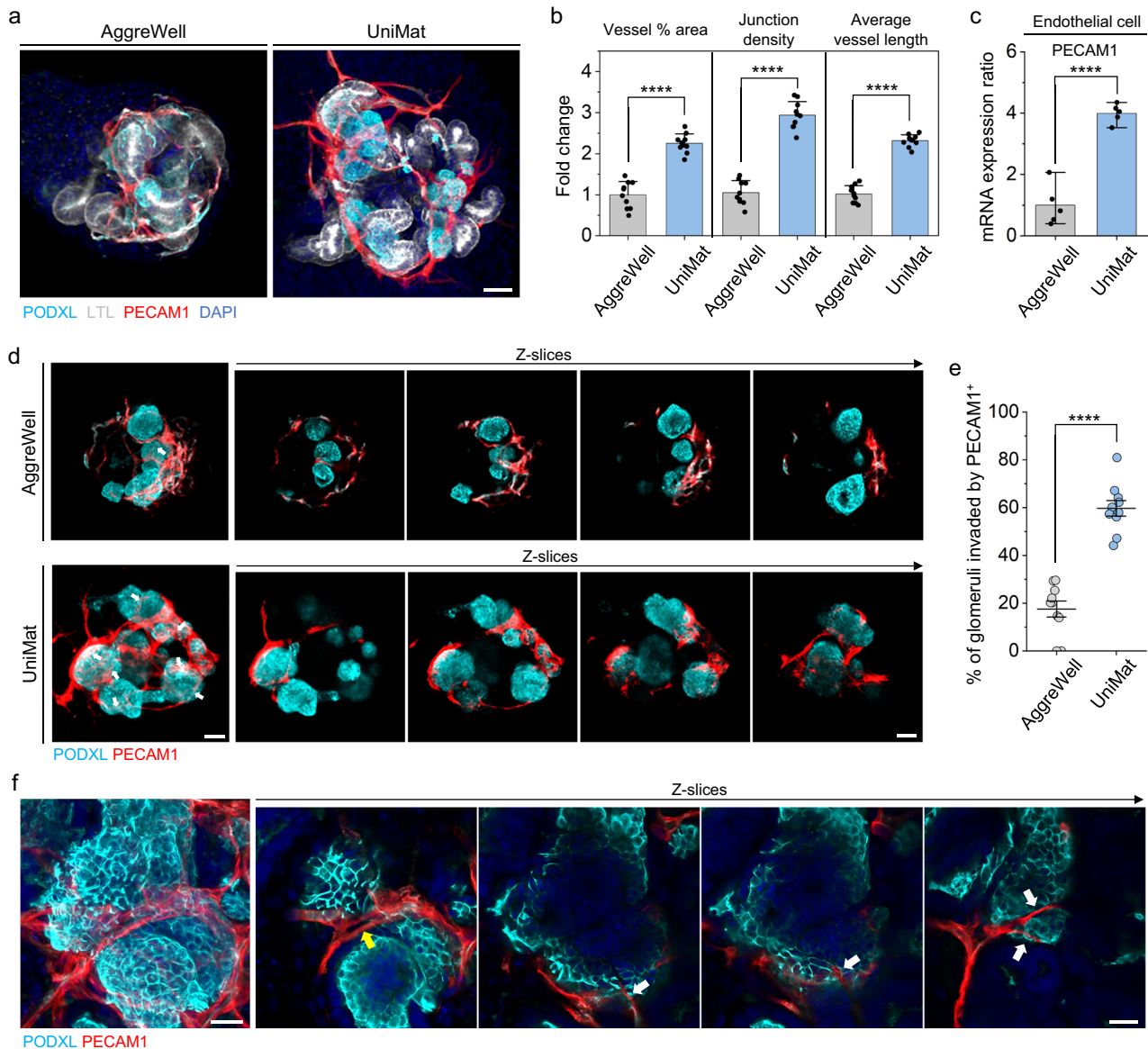


Fig. 4 | Generation of enhanced vascularized kidney organoids in UniMat.

a Confocal z-stack images for PODXL, LTL, and PECAM1 in kidney organoids cultured in AggreWell and UniMat. Scale bar = 50 μm (**b**) AngioTool outputs of abundance and character of vasculature of kidney organoids cultured in AggreWell and UniMat (reported as fold change relative to AggreWell-cultured organoids). ($n=10$ organoids, mean \pm SD). Significance by Student's t-test: $P=1.1 \times 10^{-8}$ (vessel % area), $P=7.9 \times 10^{-11}$ (junction density), $P=3.3 \times 10^{-12}$ (average vessel length). **c** qRT-PCR of PECAM1 expression of kidney organoids cultured in AggreWell and UniMat. ($n=5$ independent experiments, mean \pm SD). Significance by Student's t-test: $P=1.8 \times 10^{-5}$ (vessel % area). **d** Sequential individual confocal z-slice images of kidney organoids in

AggreWell and UniMat, stained with PODXL and PECAM1. Scale bar = 20 μm . White arrows indicate invasion of PECAM1⁺ endothelial cells into PODXL⁺ podocyte clusters. **e** Quantification of percentage of PECAM1⁺ endothelial cells invasion into a glomerular-like structure in kidney organoids cultured in AggreWell and UniMat ($n=10$ organoids, mean \pm SE). Significance by Student's t-test: $P=4.3 \times 10^{-8}$ (vessel % area). **f** High-magnification sequential individual confocal z-slice images of kidney organoids cultured in UniMat, stained with PODXL and PECAM1. Scale bar = 20 μm . Yellow arrow indicates lumen-like structure of invaded PECAM1⁺ endothelial cells and white arrows indicate invasion of PECAM1⁺ endothelial cells into PODXL⁺ podocytes clusters. Source data are provided as a Source Data file.

Specifically, the differentiation of endothelial cells in the glomerulus is largely influenced by podocytes-produced VEGFA, which is crucial for attracting endothelial precursors to the glomerulus, a key step in the development of glomerular endothelial cells⁴¹. In turn, endothelial cells secrete PDGFR β , a factor essential for the glomerular filtration function, which attracts mesangial cells⁴². In a previous study, researchers transplanted kidney organoids generated in the impermeable micro-well platform into mice to promote vascularization¹⁵. Our study aimed to determine if our UniMat could promote in vitro vascularization in kidney organoids without relying on an animal host. We observed an increase in vascularization in the kidney organoids when cultured in the UniMat, as evidenced by the increased presence of renal

vasculature (PECAM1⁺) (Fig. 4a). To quantify this vascularization, we evaluated confocal z-stack images of kidney organoids using the AngioTool⁴³ (Supplementary Fig. 10a). The vessel percent area of PECAM⁺ vasculature in the UniMat-cultured organoids exhibited an increase of over two-fold compared to the AggreWell-cultured organoids (Fig. 4b). Additionally, we found that the PECAM⁺ vasculature of UniMat-cultured organoids had more than a two-fold increase in both junctional density (i.e., branch points per unit area) and average vessel length (i.e., interjunctional distance) compared to the AggreWell-cultured organoids (Fig. 4b). qRT-PCR analysis further confirmed that UniMat-cultured kidney organoids showed the upregulated expression of PECAM1 (Fig. 4c), a mature endothelial marker⁴⁴, indicating

enhanced vascular development in these organoids. To ascertain whether the vascularization induced by a permeable environment extended to the glomerular compartments of organoids, we employed confocal imaging to quantify PODXL^+ podocyte clusters invaded by PECAMI^+ vascular structures in the kidney organoids cultured in both AggreWell and UniMat (Fig. 4d and Supplementary Movies 1 and 2). While PECAMI^+ vascular invasion into the glomerular structures was rarely observed in the AggreWell-cultured organoids (Fig. 4d, e and Supplementary Movie 1), there was a noticeable increase in PECAMI^+ vascular invasion in the UniMat culture (Fig. 4d, e and Supplementary Movie 2). Enhanced imaging at higher magnification clearly showed the PECAM^+ vasculature penetrating the podocyte cluster (Fig. 4f). Additionally, we observed lumen-like structures formed by the invaded PECAMI^+ cells, characterized as open areas without nuclei (DAPI) and surrounded by PECAMI^+ region regions⁴⁴ (Fig. 4f). Intriguingly, our analysis using confocal 3D rendering revealed that the vascular structures in the kidney organoids cultured in the AggreWell displayed the characteristics of endothelial cell precursors⁴⁵, expressing both PECAMI^+ and PODXL^+ , compared to the kidney organoid in UniMat (Supplementary Fig. 10b), suggesting an immature vascularization of organoids. These findings suggest that the vascular structures within the kidney organoids cultured in the UniMat exhibit greater development compared to those cultured in AggreWell.

Building on our results, which demonstrated enhanced vascularization in kidney organoids cultured in UniMat, we hypothesized that their functionality within the renin-angiotensin-aldosterone system (RAAS) would also be promoted in this environment^{46,47}. In kidney tissue, angiotensin-converting enzyme (ACE), a key regulator of RAAS, is highly expressed in the vascular endothelial cells and proximal tubules⁴⁸. ACE is essential for sodium and water homeostasis controlling blood pressure and fluid balance control in the body⁴⁸ and plays pivotal roles in normal kidney development⁴⁷. Using enzyme-linked immunosorbent assay (ELISA)⁴⁹, we measured ACE secretion levels in kidney organoids cultured in both systems (Supplementary Fig. 10c). Notably, ACE protein levels were 8-fold higher in UniMat compared to AggreWell (Supplementary Fig. 10c), suggesting that the UniMat environment, which promotes organoid vascularization, also enhances the functional characteristics of kidney organoids.

UniMat supports long-term stability and functionality of organoids

We extended our investigation to assess the long-term stability and functional integrity of kidney organoids cultured in UniMat over a 50-day period. Our analysis further focused on potential structural loss and the risk of fibrosis, major concerns in long-term cultured organoids^{50–52}. The findings revealed that organoids cultured in UniMat retained their mature nephron structures, as evidenced by the maintenance of PODXL^+ podocytes, LTL^+ polarized proximal tubules, and CDHI^+ distal tubules (Supplementary Fig. 11a). Mature vascular structures, indicated by PECAMI^+ , were also maintained in UniMat-cultured organoids. Additionally, these organoids exhibited higher expression of genes encoding functional markers for podocytes (NPHS1 , PODXL), proximal tubules (ABCB1 , AQP1 , SLC34A1), the loop of Henle (UMOD), distal tubules (CDHI), and endothelial cells (PECAMI) compared to AggreWell-cultured organoids (Supplementary Fig. 11b), demonstrating UniMat's capability to support the stability and functionality of organoids in long-term cultivation. While α -smooth muscle actin (αSMA), a marker for myofibroblasts elevated in the interstitial areas of fibrotic kidneys⁵³, was expressed in the UniMat-cultured organoids at day 50 (Supplementary Fig. 11c), it was localized separately from nephron structures, maintaining nephron integrity (Supplementary Fig. 11d). In contrast, AggreWell-cultured organoids exhibited αSMA^+ cells interspersed within nephron structures (Supplementary Figs. 11c, d), indicating potential structural impairment due to fibrotic changes. The low fibrotic changes in UniMat are likely due to the

adequate supply of oxygen and growth factors during long-term culture, which mitigates pro-fibrotic pathways driven by cellular senescence and hypoxia^{50–52}.

Single-cell transcriptomic profiling of kidney organoids in UniMat

To investigate the comprehensive capability of UniMat, we performed single-cell RNA sequencing (scRNA-seq) using the 10X Genomics platform and analyzed the data using the Seurat R package. We compared the kidney organoids cultured in UniMat to those cultured in the AggreWell to assess the functionality of UniMat's permeability in the maturation of kidney organoids. After implementing quality control measures, we isolated 17,412 cells from day-25 kidney organoids in AggreWell and 13,098 cells from those in UniMat. These 30,510 cells were subsequently integrated and visualized using the Uniform Manifold Approximation and Projection (UMAP). The cells were categorized into 16 distinct clusters, each of which was annotated by comparing differentially expressed genes to known markers specific for cell types (Fig. 5a). A dot plot across different clusters exhibited unique transcript expression patterns for each cluster (Fig. 5b). Notably, 11 of these clusters were identified as differentiated kidney cells: podocytes (POD ; PODXL , NPHS1 , and NPHS2)^{54,55}, early proximal tubules (EPT ; SPP1 and HPN with low LRP2 and SLC3A1 expression)^{54,55}, proximal tubules (PT ; UGT3A1 , LRP2 , and SLC3A1)⁵⁶, loop of Henle/distal tubules (LOH/DT ; MAL , WFDC2 , and EPCAM)⁵⁵, endothelial cells (EC ; PECAMI , CDH5 , and SOX17)⁵⁷, juxtglomerular cells (JG ; REN and PIP5K1B)⁵⁸, and five mesenchymal clusters (Mesen ; COL1A1 and COL4A1)^{15,55}. The proportion of differentiated kidney cells in both platforms was similar, accounting for 78.70% of the cells in UniMat and 74% in AggreWell among whole cells (Fig. 5c). The remaining cells included nephron progenitor cells (NPC), defined by expression of SIX2 and EYA1 , along with proliferative premature tubular cells (Tub.pre ; MKI67 , SPP1 , and FXVD2)^{54,59}, proliferative mesenchymal cells (Prolif.Mesen ; CENPF , COL1A1 , and COL4A1)⁵⁴, and muscle cells (Muscle ; MYPLF and MYOG)⁵⁵ (Fig. 5c).

We further examined the cell-type proportions in each kidney organoid from both AggreWell and UniMat (Supplementary Table 5 and Supplementary Fig. 12). These findings were then juxtaposed with a recently published scRNA-seq dataset for human and mouse nephrons with a focus on core nephron segments such as podocytes, broad proximal tubules (including early proximal tubules), and loop of Henle/distal tubules (Fig. 5d). In the AggreWell samples, podocytes constituted 35.74%, broad proximal tubules 48.58%, and loop of Henle/distal tubules 15.68% (Fig. 5d). This distribution aligns with prior findings using the Morizane protocol^{55,60}, which showed high percentages of podocytes and proximal tubules. Remarkably, kidney organoids from the UniMat exhibited a 4.5-fold decrease in podocytes (7.97%), but higher proportions of broad proximal tubules (60.93%) and loop of Henle/distal tubules (31.10%). These proportions more closely resemble the cellular composition of natural nephrons in both mice^{61,62} and humans^{63,64} (Fig. 5d). Significantly, within the broad proximal tubule category, the proportion of early proximal tubules was 18.7% in UniMat, as compared to 62% in AggreWell, highlighting a higher presence of mature proximal tubules in the former. The higher tubule-to-glomerulus ratio observed in UniMat-cultured kidney organoids is strongly associated with enhanced WNT4 expression—a key signaling molecule in kidney development processes such as the mesenchymal-to-epithelial transition and nephron formation^{57,65} (Supplementary Fig. 13). This elevated WNT signaling in the UniMat system is likely driven by the efficient delivery of the WNT agonist CHIR99021 (CHIR) during the critical nephron patterning stage on days 9–11 through the permeable membrane. Beyond nephron cells, there was a noticeable difference in the NPC cluster: AggreWell exhibited a fraction 1.7 times higher than that of UniMat (Fig. 5e). This further demonstrated the enhanced maturity of kidney organoids cultivated on the UniMat

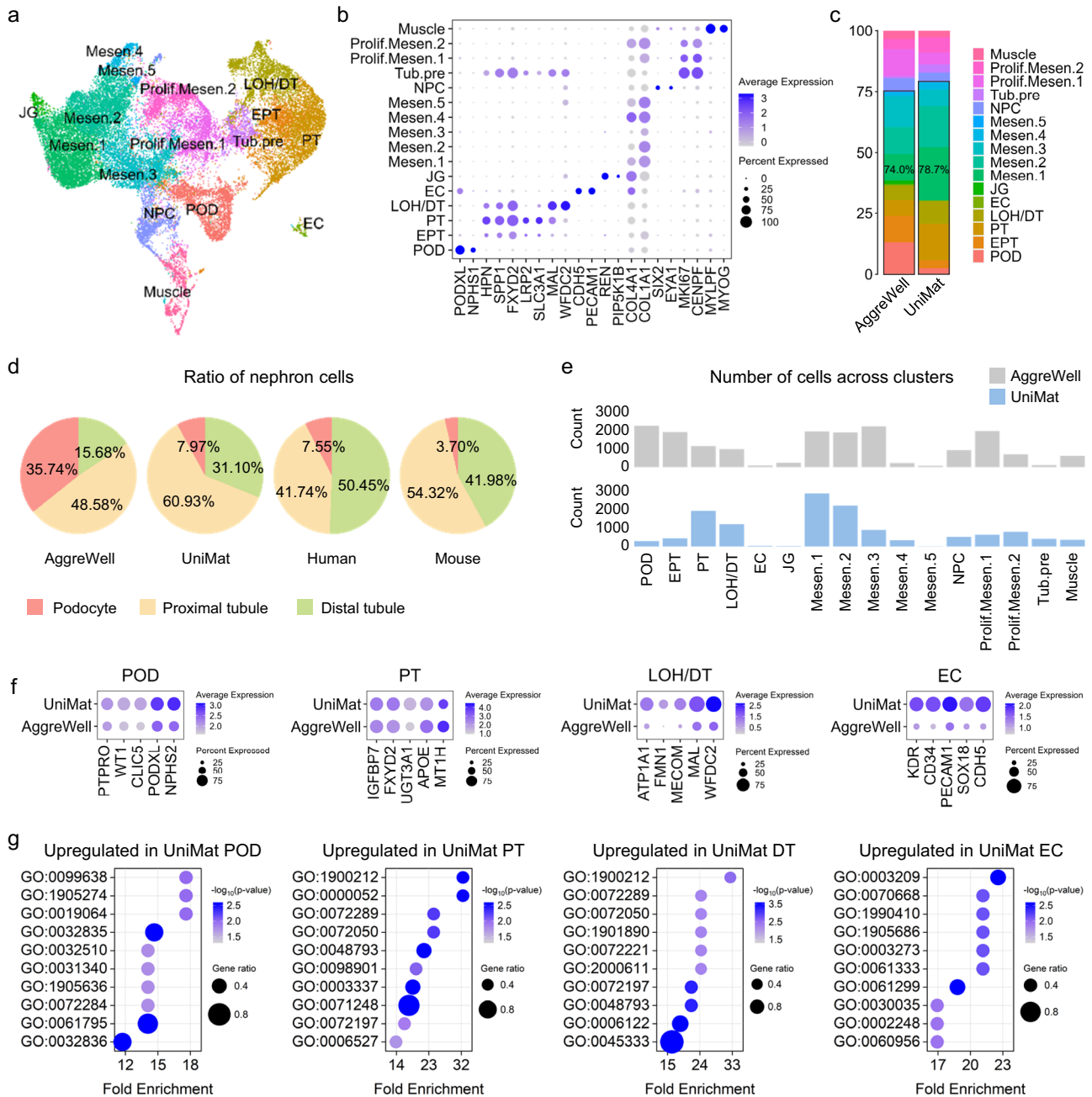


Fig. 5 | Single-cell transcriptomic profiling of kidney organoids in UniMat.

a UMAP projection of cell types annotated from 30,510 cells from kidney organoids on day 25 in both AggreWell and UniMat (POD, Podocyte; EPT, Early proximal tubule; PT, Proximal tubule; LOH/DT, Loop of Henle/Distal tubule; EC, Endothelial cell; JG, Juxtaglomerular cell; Mesen, Mesenchyme; NPC, Nephron progenitor cell; Tub.pre, Tubular precursor; Prolif.Mesen, Proliferating mesenchyme). **b** Dot plot showing expression of cell type-specific genes. **c** Bar plot presenting percentage of cells across clusters between AggreWell and UniMat. **d** Pie chart depicting ratios of podocytes, proximal tubules, and loop of Henle/distal tubules in AggreWell,

UniMat, human, and mouse datasets. Human and mouse datasets are from Lake et al. (human)⁶⁴ and Clark et al. (mouse)⁶². **e** Number of cells across clusters in AggreWell and UniMat. **f** Dot plot comparing expressions of cell type-signature genes on POD, PT, LOH/DT, and EC clusters between AggreWell and UniMat. **g** Biological Process Gene Ontology (GO) enrichment analysis of differentially expressed genes in POD, PT, LOH/DT, and EC clusters of UniMat. Significance by Fisher's Exact Test with Benjamini-Hochberg correction. Source data are provided as a Source Data file.

platform (Fig. 5e and Supplementary Table 5). Given that tissue structure and function hinge on cellular compositions, these results emphasize the greater in vivo relevance of kidney organoids generated using UniMat.

We next examined gene expression profiles of podocytes, proximal tubules, loop of Henle/distal tubules as well as endothelial cell clusters (Fig. 5f and Supplementary Fig. 14). The analysis revealed elevated expression of genes related to differentiation in the podocytes, loop of Henle/distal tubules, and endothelial cells clusters. This

suggests a greater degree of maturity in kidney organoids cultivated using the UniMat. Although the gene expression profiles in the proximal tubule cluster appeared similar between UniMat and AggreWell, a low proportion of early proximal tubules in UniMat (Supplementary Fig. 15) indicates a more mature state of these tubules.

To explore the potential pathways and functions that differentiate kidney organoids in UniMat compared to those in AggreWell, we carried out Biological Process Gene Ontology (GO) enrichment analysis on genes that were upregulated in podocytes, proximal tubules, loop

of Henle/distal tubules, and endothelial cells clusters within the UniMat (Fig. 5g). In the podocyte cluster, UniMat showed elevated expression of genes associated with glomerulus development (GO:0032835) and glomerular basement membrane development (GO:0032836) (Supplementary Table 6). For both the proximal tubule and the loop of Henle/distal tubule clusters, the most enriched GO terms were associated with the negative regulation of mesenchymal cell apoptosis in metanephros development (GO:1900212), metanephric nephron tubule formation (GO:0072289), and ureter morphogenesis (GO:0072197) (Supplementary Table 7). These observations corroborate the advanced tubular structures observed in the UniMat-cultured kidney organoids. In the loop of Henle/distal tubule cluster, enriched GO terms revealed elevated expression of genes like *CLDN3*, *CLDN19*, and *CRB3*, which are linked to the positive regulation of cell junction assembly (GO:1901890) (Supplementary Table 7). This suggests enhanced epithelial junctions in kidney organoids cultured in UniMat. Additionally, the GO term related to metanephric distal convoluted tubule development (GO:0072221) was enriched in UniMat (Supplementary Table 7), indicating a higher propensity for kidney organoids to differentiate into distal tubules in UniMat as compared to AggreWell, as shown in Fig. 5d. In the endothelial cell cluster, upregulated genes such as *SOX17*, *SOX18*, *NRP1*, and *CLIC4*, played a role in endothelial cell differentiation (GO:0060956) (Supplementary Table 8). These findings are in line with the improved development of kidney organoids in UniMat.

Potential of UniMat in standardizing organoid-based assays

While earlier researches have utilized kidney organoids to simulate polycystic kidney disease (PKD) and mimic its pathological features, the inconsistent morphology of these organoids often resulted in considerable variability in both size and cystic regions^{15,66}. Recognizing that UniMat facilitates the generation of kidney organoids with shape and functional consistency and higher maturity in tubular structures across different nephron segments, we employed these organoids for PKD modeling to evaluate UniMat's potential as a drug testing platform. To induce PKD, we chose forskolin, which serves as a direct activator of adenylyl cyclase (AC), replicating the cyclic adenosine monophosphate (cAMP)-mediated pathophysiological processes central to PKD^{67–69}. We exposed the UniMat-cultured kidney organoids to a 30 μ M concentration of forskolin for 48 h (Fig. 6a) to reproduce the elevated-cAMP levels that lead to the abnormal cystic formation characteristic of PKD's physiology. This enabled us to evaluate the platform's suitability for generating PKD organoids⁷⁰. In response to the forskolin treatment, we observed both an enlargement and the formation of cysts within organoids. This confirmed the UniMat's ability to reliably produce PKD organoids on a scalable level (Fig. 6b).

To evaluate if the uniformly mature kidney organoids generated in UniMat enhance the reliability of PKD modeling, we compared the cyst-forming features of organoids cultured in the hydrogel layer, AggreWell, and UniMat. To facilitate closer observation, the kidney organoids cultured in UniMat and AggreWell were transferred to individual ultra-low attachment plates prior to 48-h exposure to forskolin at concentrations of 10 and 30 μ M (Fig. 6a). Notably, cysts became evident within 24 h of forskolin exposure, predominantly in the LTL⁺ and CDH1⁺ tubular regions (Supplementary Fig. 16). To quantify cyst dimensions, we measured the areas of individual kidney organoids on day 26, prior to forskolin treatment, and calculated an average area to establish a baseline for the collective pre-treatment state of the organoids. After 48 h of treatment, we measured the areas of individual organoids again. The post-treatment areas were compared to the pre-treatment average, and the change was expressed as a percentage, termed percent area. This method efficiently captured the collective response of the organoid population to the treatment and simplified the quantification process by focusing on collective changes across the group rather than tracking each organoid individually. As

expected, a considerable variability in the size and morphology of kidney organoids cultured on the hydrogel layer resulted in inconsistent cyst formation, in terms of both location and dimensions (Fig. 6c). A similar pattern of variability and incomplete cyst formation was observed in organoids cultured in the AggreWell, implying the existence of undifferentiated, non-renal structures unresponsive to forskolin treatment (Fig. 6c). Additionally, cyst formation in kidney organoids from both hydrogel layer and AggreWell was erratic, regardless of forskolin dosage and time of exposure (Fig. 6e). In contrast, organoids in the UniMat exhibited uniform cysts throughout their entire structure, resulting in consistent increases in overall sizes. This trend was also observed when forskolin was directly applied to the kidney organoids within UniMat (Supplementary Fig. 17). This can be attributed to the high and consistent differentiation of nephrons. When comparing the percentage area of individual forskolin-treated PKD organoids to their average size before treatment, we found that clear dose-dependent responses were observed specifically in the UniMat (Fig. 6e).

To explore the impact of uniform disease modeling on drug testing results, we exposed PKD organoids, induced by forskolin (30 μ M), to CFTR inhibitor-172 at concentrations of 50 or 100 μ M (Fig. 6a). This PKD drug, which targets the cytoplasmic side of CFTR, had previously demonstrated its potential to inhibit cyst growth in PKD mice and in vitro models^{71,72}. The PKD organoid induced from kidney organoids cultured in UniMat displayed consistent reductions in size (Fig. 6d). The percent area, calculated in the same manner as the cyst dimensions, showed a clear dose-dependent decrease (Fig. 6f). In contrast, the PKD organoids from both hydrogel layer and AggreWell experienced inconsistent changes in cyst dimensions. Our results indicate that, within the UniMat platform, we can validate not only the formation but also the reduction of cysts by simply comparing average size changes across the organoid population, without the need to track individual organoids.

Next, we further validated the consistency and repeatability of UniMat for uniform disease modeling by implementing an acute kidney injury (AKI) model. Previous AKI organoid models have shown expression of kidney injury molecule-1 (KIM-1)^{8,73}, a selective kidney injury marker significantly upregulated in injured proximal tubules^{74,75}. However, the variability of renal injury between organoids remains a concern. To assess UniMat's suitability for uniform kidney injury induction, we exposed kidney organoids to varying concentrations of lipopolysaccharide (LPS), an endotoxin from gram-negative bacteria known to cause AKI, for 24 hours⁷⁶ (Supplementary Fig. 18a). Consistent with previous findings⁷⁷, we observed KIM-1 expression in LTL⁺ proximal tubules of organoids cultured in hydrogel layers, AggreWell, and UniMat in response to LPS (Supplementary Fig. 18c). Comparing the percentage of KIM-1⁺ area relative to the total organoid area, we found considerable variability in hydrogel layers and AggreWell (Supplementary Fig. 18b), with unpredictable KIM-1 expression levels regardless of LPS concentration. In contrast, UniMat-cultured organoids showed stable, dose-dependent KIM-1 expression (Supplementary Fig. 18b). Consistent with our PKD modeling, the variability in differentiated proximal tubular proportion in hydrogel layers and the presence of undifferentiated, non-renal structures in AggreWell complicated renal injury assessment. However, UniMat-cultured organoids, with evenly differentiated proximal tubules, allowed for precise evaluation of proximal tubular injury. In summary, these findings, including consistent cyst changes in PKD organoids, highlight UniMat's applicability as a consistent and repeatable platform for accurate disease modeling and drug testing by facilitating the uniform and mature differentiation of organoids.

Discussion

Here, we present a simple, ready-to-use 3D geometrically-engineered, permeable membrane-based organoid culture platform, called

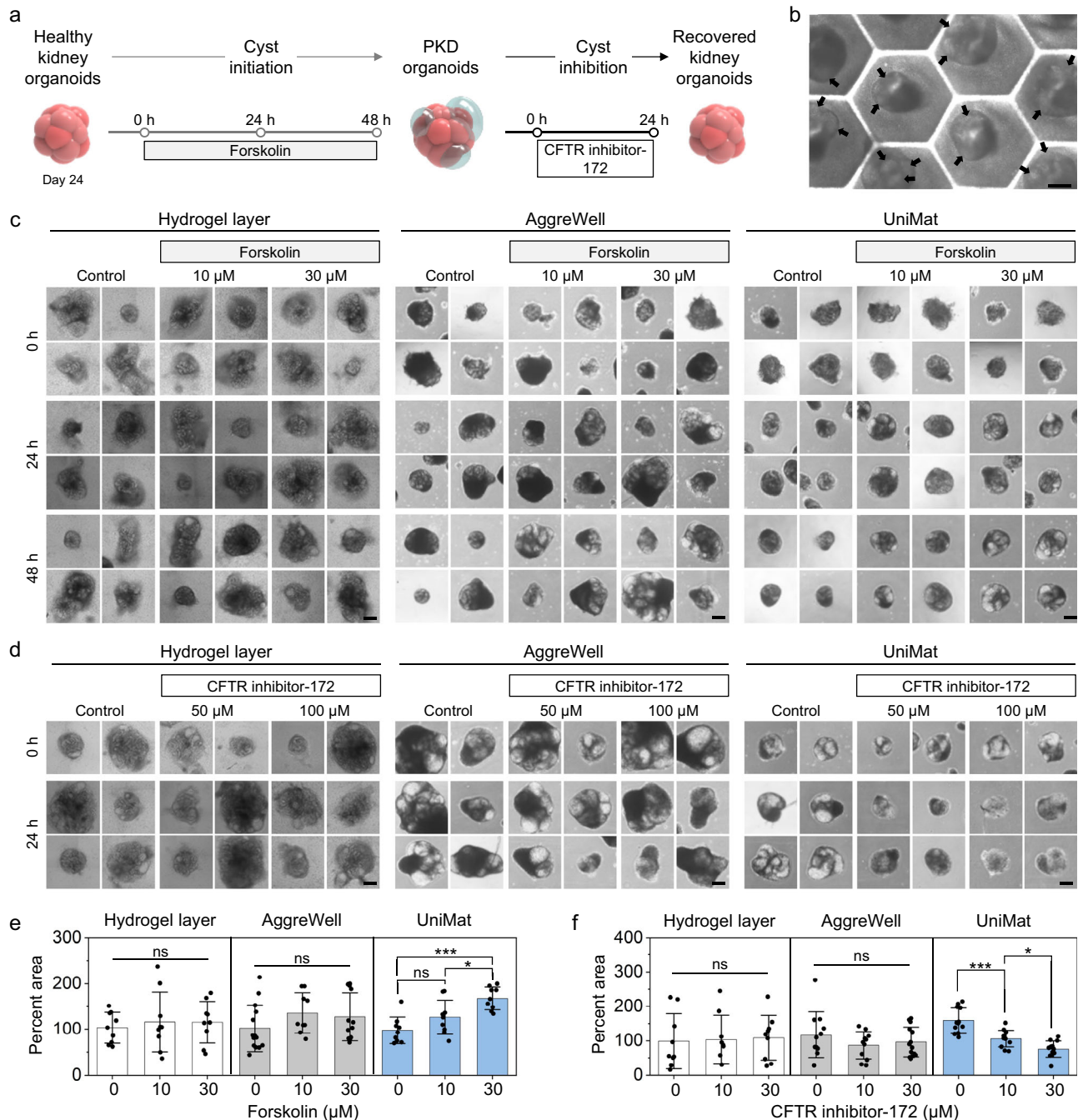


Fig. 6 | Consistency and repeatability of disease modeling and drug testing in UniMat. **a** Schematic of protocols for PKD disease modeling followed by drug testing. **b** Bright-field image of PKD organoids treated with 30 μM forskolin for 48 h in UniMat. Scale bar = 200 μm . Arrows indicate cyst formation within kidney organoids. **c** Bright-field images of individual PKD organoids induced from kidney organoids differentiated in hydrogel layer, AggreWell, and UniMat. Scale bars = 200 μm . **d** Bright-field images of individual PKD organoids treated with CFTR inhibitor-172 for 24 h, induced from kidney organoids differentiated in hydrogel layer, AggreWell, and UniMat. Scale bars = 200 μm . **e** Percent areas of individual forskolin-treated kidney organoids compared to average area of organoids before treatment from 3 independent batches. ($n = 9$ organoids for all conditions in

hydrogel layer and UniMat, and $n = 14, 9,$ and 12 organoids for AggreWell at 0, 10, and 30 μM forskolin, respectively, mean \pm SD). Significance by one-way ANOVA with Tukey's multiple comparisons test: $P_{0 \mu\text{M}, 30 \mu\text{M}} = 0.0002, P_{10 \mu\text{M}, 30 \mu\text{M}} = 0.0236$ (UniMat). **f** Percent areas of CFTR inhibitor-172-treated kidney organoids compared to average area of organoids before treatment from 3 independent batches ($n = 9$ organoids for all conditions in hydrogel layer, $n = 11, 11,$ and 14 organoids for AggreWell at 0, 10, and 30 μM forskolin, respectively, and $n = 12$ organoids for all conditions in UniMat, mean \pm SD). Significance by one-way ANOVA with Tukey's multiple comparisons test: $P_{0 \mu\text{M}, 10 \mu\text{M}} = 0.0002, P_{10 \mu\text{M}, 30 \mu\text{M}} = 0.0378$ (UniMat). Source data are provided as a Source Data file.

UniMat. This platform serves a dual purpose: it provides specific geometrical constraints on organoid growth while also facilitating an unconstrained supply of soluble factors. While previous approaches in organoid engineering have largely focused on either regulating biophysical cues^{10–12,14,15} to improve organoid uniformity or manipulating

the microenvironment to foster mature organoids^{44,78–80}, UniMat offers a notable improvement by concurrently addressing both uniformity and maturity.

Our in-depth examinations, which included confocal microscopic analysis and qRT-PCR analysis, revealed that UniMat enhances

uniformity not just in terms of physical appearance but also at the fundamental levels of structure and function of organoids when compared to those cultured on the hydrogel layer. The enhanced uniformity of kidney organoids is hypothesized to arise from the consistent initial aggregates formed within the V-shaped microwell array of the UniMat. Provided that initial cell seeding remains uniform across individual V-shaped microwells, almost consistent organogenesis and organoid formation can be anticipated. Furthermore, kidney organoids grown in the Aggrewell, a representative of impermeable microwell platforms, and those in the UniMat exhibited notable differences; the latter displayed greater structural and functional consistency (Supplementary Tables 9 and 10), even though both platforms imposed similar geometrical constraints on organoid growth. This emphasizes the crucial role of an unrestricted and spatially uniform supply of soluble factors in enhancing organoid uniformity^{78,81}. These findings show that UniMat stands out in its ability to boost organoid uniformity, a feat achieved through both its geometric design and the efficient diffusion of soluble factors. While this study showcased functional uniformity by analyzing gene expression in a group of 10 randomly selected organoids, challenges in obtaining high-purity RNA from single organoids need to be addressed for further validation of UniMat's effectiveness in promoting functional uniformity.

This study also highlights that kidney organoids matured better in the UniMat, offering a permeable environment compared to conventional microwell platforms. The UniMat facilitated an increase in the expression of nephron transcripts, as observed in both scRNA-seq and qRT-PCR analysis. Beyond the cellular level, the increased maturity was also evident in structural aspects, such as the presence of basally located ZO1⁺ tight junctions, a higher polarity of LTL⁺ proximal tubules, and enhanced vascularization, featuring a greater vascular invasion into podocytes, akin to the configuration observed in *in vivo* glomeruli. While the vascular invasion observed suggests enhanced vascularization, future studies should explore the spatial arrangement of podocytes around the invading vessels to further elucidate podocyte-vascular interactions^{82–84}. Additionally, it is important to investigate the formation of interdigitating foot processes and slit diaphragm structures between podocytes, as these are essential for glomerular filtration function^{85,86}. Confirmation of these structural features would provide deeper insights into the functional maturation of the kidney organoids.

Our scRNA-seq confirmed that kidney organoids differentiated in the UniMat exhibit a more *in vivo*-like cell-type balance of nephron elements, such as podocytes, proximal, and distal tubules, addressing the limitation of Morizane's protocol generating overpopulated podocytes and a smaller portion of tubular cells^{55,60}. Consistent with morphological findings, GO term analysis also pointed to an enrichment of genes associated with tubular morphogenesis in the UniMat-cultured organoids. We observed an enhancement of Wnt signaling related to nephron morphogenesis in the UniMat, which we partially attribute to the efficient delivery of the Wnt agonist to the NPC aggregates through the permeable membrane. Given that differences in cell-type proportions often carry biological significance, organoids developed in the UniMat could offer a more reliable nephron physiology model. Additionally, the reduction in both NPC and immature proximal tubule proportions suggests that our proposed approach accelerated kidney organoid differentiation. While recent researches have advanced kidney organoid maturity using methods like animal transplants^{33,37}, fluidic systems^{44,79}, 3D printing⁸⁸, and using decellularized ECM⁸⁴, our UniMat achieves this advancement without the need for complicated devices or drastic protocol changes. For further refinement of UniMat, a deeper exploration into its impact on the temporal molecular differentiation process of organoids is crucial.

Organoid-based tests have inherently faced challenges due to variability in organoids, particularly when used in high-throughput experiments. Specifically, for kidney organoid tests, previous research

has investigated cytotogenesis and PKD pathophysiology using non-uniform organoids. This led to inconsistent outcomes in disease modeling or pharmaceutical testing^{15,66,89,90}. As a result, the individual monitoring of cyst induction or inhibition for each organoid has become a standard protocol, adding complexity to experimental processes. By leveraging UniMat's capability to produce uniform and mature organoids, we demonstrated the potential to establish a standardized PKD model with reduced pathological heterogeneity across both organoids and batches. Our method also consistently showed responses to a PKD drug, CFTR inhibitor-172, based on dosage, a feat not achieved using conventional methods. UniMat's reliability was further confirmed through AKI modeling, showing consistent KIM-1 expression in response to LPS dosage, which allowed for the evaluation of uniform proximal tubular injury and minimized variability between organoids. Our results in both PKD and AKI modeling suggest that UniMat can consistently reproduce organoid-based assays even under different experimental conditions with varying disease types or drug concentrations. These findings indicate that UniMat could be a robust and reliable tool for nonclinical drug testing with organoids. To facilitate drug testing further, the implementation of automated measurement techniques, such as artificial intelligence (AI)-based analysis⁹¹, is essential. Such advancements are critical for conducting extensive, rapid, and high-throughput analyzes involving multiple kidney organoids cultured in UniMat, while also minimizing potential variations in measurements. Additionally, our use of forskolin as a PKD inducer in these uniformly differentiated organoids suggests the potential efficacy of other cAMP activators, such as 8-Br-cAMP^{57,89} and Prostaglandin E2 (PGE2)⁹², as chemical agents for establishing a standardized PKD model. This chemical approach could be further enhanced by utilizing genetically edited or patient-derived hiPSCs in UniMat to achieve a PKD model that closely represents genetic variations. We also expect that UniMat's capacity to enhance vascularization will allow for more precise modeling of various diseases associated with vasculopathy, such as diabetic kidney disease and nephrosclerosis⁹³.

In addition to the hydrogel and microwell arrays evaluated in this study, UniMat's distinct advantages are evident when compared to other widely used organoid culture platforms, including low-attachment culture dishes^{94,95}, spinner flasks^{96–98}, and 96-well round-bottom plates^{99–101}. While low-attachment dishes and spinner flasks facilitate scalable organoid culture with an unrestricted supply of soluble factors, they lack precise control over the organoid size and uniformity provided by UniMat^{102–104}. Moreover, although 96-well round-bottom plates are well-suited for high-content screening applications, they fall short of UniMat's efficiency and scalability in organoid production. This is due to the labor-intensive process required for individually seeding each well in 96-well round-bottom plates to produce a single organoid⁸⁸, in contrast to UniMat, where a single seeding step produces numerous organoids, reducing the effort needed to generate multiple organoids. Nonetheless, UniMat's design, which allows media sharing across microwells, presents challenges for high-content screenings on individual organoids. Additionally, light scattering from UniMat's nanofibrous structures¹⁰⁵ hinders clear microscopic observation of organoid behaviors and responses an issue not encountered in other platforms. Addressing these challenges is crucial for improving and broadening UniMat's utility.

Furthermore, UniMat has demonstrated potential as a pioneering platform for the practical applications of organoids, yet to emulate native organs more closely, strategies beyond the unconstrained supply of soluble factors are imperative. This includes simulating the complexities inherent in native organs through tissue-specific micro-environments, mechanical forces, and cellular interactions. The versatility of UniMat could be instrumental in these sophisticated applications. For example, it can be readily integrated with

microfluidic systems in a free-standing configuration (Supplementary Fig. 19), allowing for precise mechanical force stimulations for enhanced vascularization and the replication of complex cell interactions found in native tissues. Although this study demonstrated the potential of UniMat with kidney organoids, leveraging its features could enhance the maturity of various organoid models by incorporating tailored microenvironmental factors.

In conclusion, UniMat represents a notable step forward in organoid culture technology, efficiently generating organoids that are not only uniform but also mature at scale. Its potential impact on organoid technology is noteworthy, providing a practical and effective platform with broad applications across diverse biomedical research fields. Given its ability to ensure both the uniformity and maturity of organoids, UniMat could serve as a valuable tool for deepening our understanding of organ development, disease modeling, and drug screening.

Methods

Fabrication of NF membrane

For the fabrication of the electrospun NF membrane, a solution was prepared by mixing polycaprolactone (PCL; average $M_n = 80,000$ g/mol; Sigma-Aldrich) and Pluronic F108 (PF108; Sigma-Aldrich). This mixture was dissolved in 1,1,1,3,3,3-hexafluoro-2-propanol (Sigma-Aldrich) to achieve a PCL/PF108 ratio of 1:1 (w/w) and a final concentration of 8% (w/w). This solution was then loaded into a 5-ml gastight syringe (Hamilton) equipped with a 23-gauge metal needle (NanoNC) and ejected at a constant flow rate of 0.7 ml/h via a syringe pump of an electrospinning machine (ESR200R2, NanoNC). An electric voltage of 15 kV was applied between the needle and a cylindrical aluminum collector, which was positioned 14 cm below the needle. The electrospinning was conducted for 2 min, at a relative humidity of 30–40% and a temperature range of 20–25 °C, which resulted in a flat NF membrane with a thickness of 50 μm . To ensure the removal of any remaining solvent, the fabricated NF membrane underwent a further degassing step, being placed in a custom-made degassing chamber overnight.

Fabrication of UniMat and integration with well insert wall

A UniMat with a V-shaped microwell array was fabricated by a matched-mold thermoforming process²². The size of each V-shaped microwell ranged from 400 to 800 μm . A female mold, featuring the V-shaped microwell array, was manufactured via micromachining of a Polymethylmethacrylate (PMMA) substrate using a tapered end milling cutter. A male mold was subsequently prepared through polydimethylsiloxane (PDMS) replica molding against this PMMA female mold. The male mold was fixed beneath the top plate of a customized thermoforming machine, which was connected to a motorized stage. For the thermoforming process, the electrospun NF membrane, after preheating at 60 °C, was placed on the female mold. It was then microstructured via a linear movement of the male mold exerting a force of 4.8 N. Following this process, the fabricated 3D geometrically-engineered NF membrane was finally integrated into the bottom opening of a custom-made 24-well insert wall, which was produced using an injection molding machine (Sumitomo, SE50D), to finally fabricate a UniMat-integrated 24-well insert.

Scanning electron microscopy (SEM) analysis

The UniMat was sputter-coated with Pt for 180 s at an electric current of 10 mA. The geometry and structure of the UniMat were examined by SEM imaging using a field-emission scanning electron microscope (SU660, Hitachi) at an accelerating voltage of 15 kV.

Permeability measurement

Permeability was evaluated by measuring the diffusion of Lucifer yellow (Invitrogen™), and FITC-dextran tracers (3 kDa, 10 kDa, and

40 kDa; Sigma Aldrich) across the membrane. A commercially available 24-well Transwell insert with a 0.4 μm pore PET membrane (surface area of membrane = 0.33 cm^2 ; Corning) and the UniMat400-integrated 24-well insert (surface area of UniMat400 = 0.38 cm^2 , while the projection area was 0.33 cm^2) were placed in a 24-well plate. Subsequently, 0.6 ml of phosphate-buffered saline (PBS) was added to the basolateral side, and 0.1 ml of 200 $\mu\text{g}/\text{ml}$ Lucifer yellow or FITC-dextran tracer was introduced to the apical side. After a 1-h incubation at 37 °C, the solution from the basolateral side was collected, and the concentration of the Lucifer yellow or dextran tracer was determined using a microplate reader (VICTOR3, Wazobia Enterprise). The permeability coefficient (P_{app}) was calculated using the following equation:

$$P_{\text{app}} = \frac{dQ}{dt} \times \frac{1}{AC_0}, \quad (1)$$

where dQ/dt is the diffusive transport rate of Lucifer yellow or FITC-dextran, A is the surface area of the membrane, and C_0 is the initial concentration of the solution on the apical side¹⁰⁶.

Characterization of PCL/PF108 NF membrane

The hydrophilicity of the NF membranes was evaluated by measuring the water contact angle using the sessile drop method. Specifically, a 10 μl water droplet was carefully placed on the membrane surface, and the contact angle was recorded using an automated system (Smart-Drop, Femtobiomed). The light transmittance of the membranes in a wet state was also assessed using a spectrophotometer (Epoch2, Bio-Tek Instrument) across a wavelength range of 360–700 nm. Membrane thickness was gauged with a digital micrometer (QuantuMike IP65, Mitutoyo). Additionally, the diameter of the electrospun nanofibers was analyzed using ImageJ software (NIH), based on SEM images of the membranes.

hiPSC culture

In this study, the WTC-11 hiPSC cell line (male; GM25256, Coriell Institute for Medical Research) and the IMR90-4 hiPSC cell line (female; WISCi004-B, WiCell) were utilized. Both cell lines were authenticated through karyotypic analysis by the Coriell Institute for Medical Research and WiCell, respectively. The WTC-11 hiPSC was maintained under feeder-free conditions on 1% GelTrex (A1413302, Thermo Fisher Scientific)-coated 6-well cell culture plates using mTeSR™1 (85850, Stem Cell Technologies) in a 37 °C incubator with 5% CO_2 . The hiPSCs were passaged every 4 days using ReLeSR™ (05872, Stem Cell Technologies) according to the manufacturer's protocol. For all experiments, hiPSCs from passages 45 to 70 were used. The IMR90-4 hiPSC cell line was also maintained in 1% GelTrex-coated 6-well cell culture plates using mTeSR™1. These cells were passaged every 3–4 days using Versene Solution (15040066, Thermo Fisher Scientific) as per the manufacturer's protocol.

Differentiation of hiPSCs into nephron progenitor cells (NPCs)

hiPSCs were differentiated into NPCs using our optimized kidney organoid differentiation protocol, which was developed based on a previously reported protocol²⁸. Briefly, hiPSCs, which were singularized using Accutase (07920, Stem Cell Technologies), were plated at a density of $\sim 235,000$ cells/well in a 6-well plate in mTeSR™1 supplemented with a 10 μM ROCK inhibitor Y27632 (1254, Tocris Bioscience). Once the confluency of the hiPSCs reached about 50%, the cells were treated with CHIR99021 (8–10 μM ; 4423, TOCRIS) and Noggin (10 ng/ml; 120–10 C, Peprotech) in a basal differentiation medium, which consisted of Advanced RPMI 1640 (12633-020, Thermo Fisher Scientific) and GlutaMAX (35050-061, Thermo Fisher Scientific), for 4 days. On day 4, the medium was replaced with the basal differentiation medium containing Activin A (10 ng/ml; 338-AC,

R&D Systems), and on day 7, it was replaced with the medium containing FGF9 (10 ng/ml; 100-23, Peprotech). After a 48-hour treatment with FGF9, the cells were differentiated into NPCs.

Generation of kidney organoids

For generating kidney organoids in UniMat, the sterilized UniMat was coated with 0.025% agarose (A4018, Thermo Fisher Scientific), which was optimized not to maintain the permeability and structural integrity of the UniMat (Supplementary Fig. 20), for 12 h to improve the low attachment condition at the bottom of UniMat. On day 9, the dissociated NPCs were seeded into UniMat400, UniMat600, and UniMat800 at a density of 5000, 11,000, and 20,000 cells per individual microwell, respectively, with the basal differentiation medium containing 3 μ M CHIR and 10 ng/ml FGF9. After 2 days, the medium was switched to the basal differentiation medium but supplemented with 30 ng/ml FGF9 and 1.5% FBS. On day 14, the medium was replaced with the medium containing 1.5% FBS, and from day 14 to 25, cultures were maintained in the basal differentiation medium with 1.5% FBS. The same procedure was also applied to AggreWell™ Microwell Plates (AggreWell™800, Stem Cell Technologies), which were pre-treated with an AggreWell™ Rinsing Solution (07010, Stem Cell Technologies) according to the manufacturer's protocol, where a cell seeding density was 15,000 cells per individual microwell. This seeding density ensured stable initial aggregate formation within AggreWell, comparable in size to those in UniMat (Supplementary Fig. 21), thereby standardizing the initial stage for subsequent organoid differentiation. To further minimize potential variations in the organoid differentiation process, we adjusted the media volume to $625 \times 10^6 \mu$ l per cell across both platforms.

Immunofluorescence imaging

After washing organoids with DPBS (LB001-01, Welgene), the organoids were fixed in 4% paraformaldehyde for 1 h at room temperature. After washing the samples with PBS three times, they were blocked overnight at 4 °C with 1 vol% donkey serum (Sigma-Aldrich) in PBS with 0.125 vol% Triton X-100. Then, primary antibodies were incubated with the samples for 2 days at 4 °C at the dilutions listed in Supplementary Table 11 in a solution of 0.5 wt% bovine serum albumin (BSA) and 0.1 vol% Triton X-100. After washing for 1 day with a solution of 0.5 wt% BSA and 0.1 vol% Triton X-100 in PBS, secondary antibodies were incubated for 3 h at a 1:500 dilution in a solution of 0.5 wt% BSA and 0.1 wt% Triton X-100 in PBS. After washing for 1 day with a solution of 0.5 wt% BSA and 0.1 vol% Triton X-100 in PBS, samples were counter-stained with 4',6-diamidino-2-phenylindole (DAPI; D9542, Sigma-Aldrich) at a 1:1000 dilution for 1 h and then washed with PBS. Before imaging, the stained organoids were cleared with fructose–glycerol clearing solution¹⁰⁷. The clearing solution was prepared by mixing 33 ml of glycerol (G2025, Sigma-Aldrich), 7 ml of distilled water, and 29.72 g of fructose (F0127, Sigma-Aldrich), followed by stirring the mixture on a magnetic stirrer. The prepared solution was then applied to the samples. Images were taken using a confocal microscope (FV3000, Olympus). The antibodies used in this study are listed in Supplementary Table 11.

Image analysis and quantification

To analyze the area of kidney organoids, bright-field images of organoids were acquired on a microscope (Carl Zeiss). Image reconstruction of the z-stacks of bright-field images was generated using Mosaic 2.0 (Tucsen). Kidney organoids were randomly selected for all experiments. The area of kidney organoid was determined by manually outlining z-projected images using the freehand selection tool in ImageJ software (NIH). The projected distances of the organoid center from the microwell center were determined by manually drawing a line from the microwell center to the organoid center on z-projected bright-field images. These distances were then analyzed using ImageJ

software (NIH). To quantify the volume of PODXL⁺, LTL⁺, and CDH1⁺ cells within the kidney organoids, confocal z-stacks of PODXL, LTL, and CDH1 were acquired, ensuring that these z-stacks were taken at the maximal limit of the confocal depth for each sample. These z-stack images were then imported into the Imaris imaging software, where confocal 3D renderings were generated to delineate glomerular and tubular volumes. The Imaris software was subsequently employed to quantitatively assess the volume occupied by PODXL⁺, LTL⁺, and CDH1⁺ cells.

Quantitative real-time polymerase chain reaction (qRT-PCR)

Kidney organoids were extracted from the hydrogel layer, the AggreWell, or the UniMat using a pipette. RNA was isolated from the organoid samples using the ReliaPrep™ RNA Miniprep Systems (Promega), as per the manufacturer's protocol. cDNA was synthesized with a cDNA synthesis kit (K1641, Thermo Fisher Scientific) according to the manufacturer's protocol. qRT-PCR was carried out with Power SYBR® Green Master Mix (Applied Biosystems™) on a StepOnePlus™ Real-Time PCR System (Applied Biosystems™). Relative mRNA expression levels were normalized to glyceraldehyde 3-phosphate dehydrogenase (GAPDH) expression and analyzed by the $2^{-\Delta\Delta Ct}$ method. Sequences of the primers used in this study are listed in Supplementary Table 12.

Dextran uptake assay

The kidney organoids cultured in both UniMat and AggreWell were incubated with 100 μ g/ml of 10,000 M_w cascade blue-labeled dextran (D1976, Thermo Fisher Scientific) in the basal differentiation medium for 24 h. After this period, the medium was replaced with the fresh basal differentiation medium without dextran and incubated for an additional 24 h. Subsequently, the organoids were fixed with PFA 4% and stained with LTL.

Live/dead cell assay of NPCs

The viability of NPCs was assessed using a live/dead assay kit (L3224, Invitrogen). Aggregates of NPCs cultured in both UniMat and AggreWell were washed with DPBS and treated with a staining solution containing 0.5 μ l/ml calcein-AM and 2 μ l/ml of 3 mM ethidium homodimer-1 (EthD-1) in PBS for 30 min at room temperature. Following staining, the aggregates were rinsed with PBS. Stained aggregates were immediately imaged using the confocal microscope. The fluorescence images were then imported into ImageJ software for quantification of the percentage of dead cells. The percentage of dead cells was calculated by dividing the total red fluorescence intensity by the sum of the total green fluorescence intensity and the total red fluorescence intensity and then multiplying by 100.

Numerical simulation of glucose concentration

The spatiotemporal distribution of glucose concentration around the kidney organoid situated in a single microwell was numerically simulated using COMSOL Multiphysics software (Ver. 5.0, COMSOL). This model simulated the diffusive transport of diluted glucose species in response to glucose consumption by the organoid. The geometries and dimensions were designed to match to those of the corresponding experimental setup. The parameters used for this simulation are listed in Supplementary Table 13.

ELISA of ACE

The culture medium from organoids was collected over a period of 7 days since day 21, centrifuged, and analyzed with Human ACE/angiotensin-converting enzyme 1 ELISA kit (HUF100025, AssayGenie), following the manufacturer's instructions. The quantification of ACE protein was then normalized to the number of cells counted in each sample.

Single-cell RNA sequencing and data processing

Kidney organoids were collected from both the AggreWell and UniMat using a pipette and then dissociated into single cells using Accutase at 37 °C for 20 min. The single cells were resuspended in the basal differentiation medium containing 1.5% FBS. After singularization, samples were prepared following the manufacturer's protocol (10X Genomics). The single-cell libraries were sequenced using the Chromium Next GEM Single Cell 3' RNA library and gel bead v3.1 kit in HiSeqXten (Illumina). Alignment to the GRCh38 human reference genome, filtering, barcode counting, and UMI counting of FASTQ files was performed using the Cell Ranger (v6.1.2) pipeline (10X Genomics). Pre-processing of raw scRNA-seq data was carried out by MacroGen, Inc.

Analysis of scRNA-seq data

The output from Cell Ranger was imported into R (v4.3.1) and Seurat (v4.3.0.1) for downstream analyzes. Cells expressing fewer than 200 genes, more than 6000 genes, or with over 10% of reads assigned to mitochondrial genes were excluded. After this quality control step, we retained a total of 30,510 cells, comprising 17,412 cells from AggreWell and 13,098 cells from UniMat. We normalized each dataset and identified highly variable features using the `NormalizeData` and `FindVariableFeatures` functions, respectively. The two Seurat objects were combined using canonical correlation analysis (CCA) through the `IntegrateData` function, following the workflow proposed by the Satija group¹⁰⁸. Principal component analysis was carried out using the `RunPCA` function, and the results were employed for clustering with the `FindNeighbors` and `FindClusters` functions. The UMAP projection was generated using the `RunUMAP` function. In total, cells were classified into 16 distinct clusters. Each of these clusters was annotated based on differential expression testing performed using the `FindAllMarkers` function with the Wilcoxon Rank Sum test. The enriched biological processes of the upregulated genes in each cluster were analyzed using the DAVID database¹⁰⁹.

PKD modeling and drug testing

In situ PKD modeling of kidney organoids within UniMat was carried out by introducing the basal differentiation medium containing 30 μM forskolin (F-9929, LC Laboratories) directly to the UniMat for 48 h. Cytogenesis initiation in the kidney organoid was achieved upon treatment of forskolin. For PKD organoid modeling, kidney organoids cultured in both the UniMat and AggreWell were individually transferred to ultra-low attachment 6-well plates (3471, Corning). Subsequently, they were exposed to forskolin (10 and 30 μM) for 48 h. Inhibition of cytogenesis was achieved by treating CFTR inhibitor-172 (HY-16671, MedChemExpress). After a 48 h treatment with 30 μM forskolin, CFTR inhibitor-172 was introduced at concentrations of 50 and 100 μM in the medium with 30 μM forskolin for an additional 24 h. For the case of the hydrogel layer, both cyst induction and inhibition were carried out by changing the medium containing forskolin and CFTR inhibitor-172, respectively, in an in-situ manner. The concentrations of forskolin⁶⁶ and CFTR inhibitor-172⁵⁷ were determined based on the previous studies. The percent area was calculated by comparing the area of individual organoids treated with either forskolin or CFTR inhibitor-172 to the average area of original or forskolin-treated organoids, respectively. The calculation formula is as follows:

$$\text{Percent area} = \left(\frac{\text{Individual organoid area after treatment}}{\text{Average of organoid areas before treatment}} \right) \times 100. \quad (2)$$

Areas of organoids were quantified using the polygonal selection tool in ImageJ software (NIH).

LPS-induced AKI modeling

Kidney organoids cultured in a hydrogel layer, AggreWell, and UniMat were exposed to 1 and 10 μg/ml LPS (L4391, Sigma-Aldrich). After 24 h, organoids were fixed with PFA 4% and stained with KIM-1 and LTL. To evaluate the variability of KIM-1 expression relative to the total organoid area, the KIM-1⁺ and DAPI⁺ area for each organoid was analyzed using ImageJ (NIH). The percentage of the KIM-1⁺ area was calculated by dividing the KIM-1⁺ area by the DAPI⁺ area and then multiplying the result by 100.

Statistics and reproducibility

The sample size for each experiment was determined based on a minimum of $n = 3$ independent samples for every experimental group. No data were excluded from analyzes. All experimental assays were performed in at least three independent replicates, with successful replication in all cases. Samples were randomly selected when multiple samples were used for experiments. Statistical analyzes were carried out using the Student's t-test for comparing two data sets and a one-way analysis of variance (ANOVA) with Tukey's multiple comparisons test for evaluating differences among multiple data sets. For single-cell RNA-seq data, GO term enrichment was analyzed using the DAVID tool, with significance determined by Fisher's Exact Test and Benjamini-Hochberg correction for multiple comparisons. Data are presented as mean ± SD (standard deviation), except for Fig. 4e, where data are presented as mean ± SE (standard error). Significance levels are denoted by one asterisk for P -values < 0.05, two asterisks for P -values < 0.01, three asterisks for P -values < 0.001, and four asterisks for P -values < 0.0001.

Reporting summary

Further information on research design is available in the Nature Portfolio Reporting Summary linked to this article.

Data availability

The scRNA-seq data generated in this study have been deposited in the NCBI Gene Expression Omnibus under accession number [GSE252104](https://www.ncbi.nlm.nih.gov/geo/query/acc.cgi?acc=GSE252104). All other data supporting the findings of this study are available within the article and its supplementary files. Any additional requests for information can be directed to the corresponding authors and will be fulfilled within 2 weeks. Source data are provided with this paper.

References

- Lancaster, M. A. & Knoblich, J. A. Organogenesis in a dish: modeling development and disease using organoid technologies. *Science* **345**, 124712 (2014).
- Clevers, H. Modeling development and disease with organoids. *Cell* **165**, 1586–1597 (2016).
- Dutta, D., Heo, I. & Clevers, H. Disease modeling in stem cell-derived 3D organoid systems. *Trends Mol. Med.* **23**, 393–410 (2017).
- Rossi, G., Manfrin, A. & Lutolf, M. P. Progress and potential in organoid research. *Nat. Rev. Genet.* **19**, 671–687 (2018).
- Hofer, M. & Lutolf, M. P. Engineering organoids. *Nat. Rev. Mater.* **6**, 402–420 (2021).
- Brassard, J. A. & Lutolf, M. P. Engineering stem cell self-organization to build better organoids. *Cell Stem Cell* **24**, 860–876 (2019).
- Kozłowski, M. T., Crook, C. J. & Ku, H. T. Towards organoid culture without Matrigel. *Commun. Biol.* **4**, 1387 (2021).
- Morizane, R. et al. Nephron organoids derived from human pluripotent stem cells model kidney development and injury. *Nat. Biotechnol.* **33**, 1193–1200 (2015).
- Dahl-Jensen, S. & Grapin-Botton, A. The physics of organoids: a biophysical approach to understanding organogenesis. *Development* **144**, 946–951 (2017).
- Jung, Y. H. et al. Drug screening by uniform patient derived colorectal cancer hydro-organoids. *Biomaterials* **276**, 121004 (2021).

11. Wiedenmann, S. et al. Single-cell-resolved differentiation of human induced pluripotent stem cells into pancreatic duct-like organoids on a microwell chip. *Nat. Biomed. Eng.* **5**, 897–913 (2021).
12. Loebel, C. et al. Microstructured hydrogels to guide self-assembly and function of lung alveolospheres. *Adv. Mater.* **34**, 2202992 (2022).
13. Chen, C., Rengarajan, V., Kjar, A. & Huang, Y. A matrigel-free method to generate matured human cerebral organoids using 3D-Printed microwell arrays. *Bioact. Mater.* **6**, 1130–1139 (2021).
14. Brandenberg, N. et al. High-throughput automated organoid culture via stem-cell aggregation in microcavity arrays. *Nat. Biomed. Eng.* **4**, 863 (2020).
15. Tran, T. et al. A scalable organoid model of human autosomal dominant polycystic kidney disease for disease mechanism and drug discovery. *Cell Stem Cell* **29**, 1083 (2022).
16. Lee, G. et al. Enhanced oxygen permeability in membrane-bottomed concave microwells for the formation of pancreatic islet spheroids. *Acta Biomater.* **65**, 185–196 (2018).
17. He, J. Y. et al. Scalable formation of highly viable and functional hepatocellular carcinoma spheroids in an oxygen-permeable microwell device for anti-tumor drug evaluation. *Adv. Health Mater.* **11**, e2200863 (2022).
18. Ornoff, D. M., Wang, Y. L., Proctor, A., Shah, A. S. & Allbritton, N. L. Co-fabrication of chitosan and epoxy photoresist to form microwell arrays with permeable hydrogel bottoms. *Biomaterials* **74**, 77–88 (2016).
19. Jun, Y. et al. In vivo-mimicking microfluidic perfusion culture of pancreatic islet spheroids. *Sci. Adv.* **5**, eaax4520 (2019).
20. Payne, M. C. et al. Microwell-based flow culture increases viability and restores drug response in prostate cancer spheroids. *Biotechnol. J.* **18**, e2200434 (2023).
21. Ma, L. D. et al. Design and fabrication of a liver-on-a-chip platform for convenient, highly efficient, and safe in situ perfusion culture of 3D hepatic spheroids. *Lab Chip* **18**, 2547–2562 (2018).
22. Kim, D. et al. A deep and permeable nanofibrous oval-shaped microwell array for the stable formation of viable and functional spheroids. *Biofabrication* **13**, 035050 (2021).
23. Li, Z. B. & Tan, B. H. Towards the development of polycaprolactone based amphiphilic block copolymers: molecular design, self-assembly and biomedical applications. *Mat. Sci. Eng. C. -Mater.* **45**, 620–634 (2014).
24. Azari, A., Golchin, A., Mahmoodinia Maymand, M., Mansouri, F. & Ardeshirylajimi, A. Electrospun polycaprolactone nanofibers: current research and applications in biomedical application. *Adv. Pharm. Bull.* **12**, 658–672 (2022).
25. Vasita, R., Mani, G., Agrawal, C. M. & Katti, D. S. Surface hydrophilization of electrospun PLGA micro-/nano-fibers by blending with Pluronic® F-108. *Polymer* **51**, 3706–3714 (2010).
26. Mirhosseini, M. M., Haddadi-Asl, V. & Zargarian, S. S. Fabrication and characterization of hydrophilic poly(ϵ -caprolactone)/pluronic P123 electrospun fibers. *J. Appl. Polym. Sci.* **133**, 43345 (2016).
27. Kim, D., Eom, S., Park, S. M., Hong, H. & Kim, D. S. A collagen gel-coated, aligned nanofiber membrane for enhanced endothelial barrier function. *Sci. Rep. -Uk* **9**, 14915 (2019).
28. Morizane, R. & Bonventre, J. V. Generation of nephron progenitor cells and kidney organoids from human pluripotent stem cells. *Nat. Protoc.* **12**, 195–207 (2017).
29. Schnabel, E., Anderson, J. M. & Farquhar, M. G. The tight junction protein Zo-1 is concentrated along slit diaphragms of the glomerular epithelium. *J. Cell Biol.* **111**, 1255–1263 (1990).
30. Freedman, B. S. et al. Modelling kidney disease with CRISPR-mutant kidney organoids derived from human pluripotent epiblast spheroids. *Nat. Commun.* **6**, 8715 (2015).
31. Kestila, M. et al. Positionally cloned gene for a novel glomerular protein - nephrin - is mutated in congenital nephrotic syndrome. *Mol. Cell* **1**, 575–582 (1998).
32. Nielsen, J. S. & McNagny, K. M. The role of podocalyxin in health and disease. *J. Am. Soc. Nephrol.* **20**, 1669–1676 (2009).
33. van den Berg, C. W. et al. Renal subcapsular transplantation of psc-derived kidney organoids induces neo-vasculogenesis and significant glomerular and tubular maturation in vivo. *Stem Cell Rep.* **10**, 751–765 (2018).
34. Nielsen, S. et al. Aquaporins in the kidney: from molecules to medicine. *Physiol. Rev.* **82**, 205–244 (2002).
35. Biber, J., Hernando, N., Forster, I. & Murer, H. Regulation of phosphate transport in proximal tubules. *Pflug. Arch. Eur. J. Phy* **458**, 39–52 (2009).
36. Yin, J. & Wang, J. N. Renal drug transporters and their significance in drug-drug interactions. *Acta Pharm. Sin. B* **6**, 363–373 (2016).
37. Devuyst, O., Bochud, M. & Olinger, E. and the architecture of kidney disease. *Pflug. Arch. Eur. J. Phy* **474**, 771–781 (2022).
38. Devuyst, O. & Bochud, M. Uromodulin, kidney function, cardiovascular disease, and mortality. *Kidney Int* **88**, 944–946 (2015).
39. Morizane, R. & Bonventre, J. V. Kidney organoids: a translational journey. *Trends Mol. Med* **23**, 246–263 (2017).
40. Grebenyuk, S. & Ranga, A. Engineering organoid vascularization. *Front Bioeng. Biotech.* **7**, 39 (2019).
41. Ballermann, B. J. Glomerular endothelial cell differentiation. *Kidney Int.* **67**, 1668–1671 (2005).
42. Kim, A. D. et al. Cellular recruitment by podocyte-derived pro-migratory factors in assembly of the human renal filter. *IScience* **20**, 402 (2019).
43. Zudaire, E., Gambardella, L., Kurcz, C. & Vermeren, S. A computational tool for quantitative analysis of vascular networks. *Plos One* **6**, e27385 (2011).
44. Homan, K. A. et al. Flow-enhanced vascularization and maturation of kidney organoids in vitro. *Nat. Methods* **16**, 255 (2019).
45. Sequeira-Lopez, M. L. S. & Torban, E. New insights into precursors of renal endothelium. *Kidney Int* **90**, 244–246 (2016).
46. Remuzzi, G., Perico, N., Macia, M. & Ruggenti, P. The role of renin-angiotensin-aldosterone system in the progression of chronic kidney disease. *Kidney Int. Suppl.* **68**, S57–S65 (2005).
47. Sparks, M. A., Crowley, S. D., Gurley, S. B., Mirosos, M. & Coffman, T. M. Classical Renin-Angiotensin system in kidney physiology. *Compr. Physiol.* **4**, 1201–1228 (2014).
48. Alhenc-Gelas, F., Baussant, T., Hubert, C., Soubrier, F. & Corvol, P. The angiotensin converting enzyme in the kidney. *J. Hypertens. Suppl.* **7**, S9–S13 (1989). discussion S14.
49. Pode-Shakked, N. et al. RAAS-deficient organoids indicate delayed angiogenesis as a possible cause for autosomal recessive renal tubular dysgenesis. *Nat. Commun.* **14**, 8159 (2023).
50. Akbari, S. et al. Robust, long-term culture of endoderm-derived hepatic organoids for disease modeling. *Stem Cell Rep.* **13**, 627–641 (2019).
51. Georgakopoulos, N. et al. Long-term expansion, genomic stability and in vivo safety of adult human pancreas organoids. *Bmc Dev. Biol.* **20**, 4 (2020).
52. Yengej, F. A. Y. et al. Tubuloid culture enables long-term expansion of functional human kidney tubule epithelium from iPSC-derived organoids. *Proc. Natl. Acad. Sci. USA.* **120**, e2216836120 (2023).
53. LeBleu, V. S. et al. Origin and function of myofibroblasts in kidney fibrosis. *Nat. Med.* **19**, 1047–1054 (2013).
54. Kim, J. W. et al. Kidney decellularized extracellular matrix enhanced the vascularization and maturation of human kidney organoids. *Adv. Sci. (Weinh.)* **9**, e2103526 (2022).

55. Wu, H. et al. Comparative analysis and refinement of human PSC-derived kidney organoid differentiation with single-cell transcriptomics. *Cell Stem Cell* **23**, 869–881 e868 (2018).
56. Uchimura, K., Wu, H., Yoshimura, Y. & Humphreys, B. D. Human pluripotent stem cell-derived kidney organoids with improved collecting duct maturation and injury modeling. *Cell Rep.* **33**, 108514 (2020).
57. Low, J. H. et al. Generation of human PSC-derived kidney organoids with patterned nephron segments and a De Novo vascular network. *Cell Stem Cell* **25**, 373–387 e379 (2019).
58. Lake, B. B. et al. An atlas of healthy and injured cell states and niches in the human kidney. *Nature* **619**, 585–594 (2023).
59. Combes, A. N., Zappia, L., Er, P. X., Oshlack, A. & Little, M. H. Single-cell analysis reveals congruence between kidney organoids and human fetal kidney. *Genome Med.* **11**, 3 (2019).
60. Wilson, S. B. et al. DevKidCC allows for robust classification and direct comparisons of kidney organoid datasets. *Genome Med.* **14**, 19 (2022).
61. Chen, L. et al. Renal-tubule epithelial cell nomenclature for single-cell rna-sequencing studies. *J. Am. Soc. Nephrol.* **30**, 1358–1364 (2019).
62. Clark, J. Z. et al. Representation and relative abundance of cell-type selective markers in whole-kidney RNA-Seq data. *Kidney Int.* **95**, 787–796 (2019).
63. McEvoy, C. M. et al. Single-cell profiling of healthy human kidney reveals features of sex-based transcriptional programs and tissue-specific immunity. *Nat. Commun.* **13**, 7634 (2022).
64. Lake, B. B. et al. A single-nucleus RNA-sequencing pipeline to decipher the molecular anatomy and pathophysiology of human kidneys. *Nat. Commun.* **10**, 2832 (2019).
65. Halt, K. & Vainio, S. Coordination of kidney organogenesis by Wnt signaling. *Pediatr. Nephrol.* **29**, 737–744 (2014).
66. Czerniecki, S. M. et al. High-throughput screening enhances kidney organoid differentiation from human pluripotent stem cells and enables automated multidimensional phenotyping. *Cell Stem Cell* **22**, 929–940 e924 (2018).
67. Ye, M. & Grantham, J. J. The secretion of fluid by renal cysts from patients with autosomal-dominant polycystic kidney-disease. *N. Engl. J. Med.* **329**, 310–313 (1993).
68. Torres, V. E. & Harris, P. C. Strategies targeting cAMP signaling in the treatment of polycystic kidney disease. *J. Am. Soc. Nephrol.* **25**, 18–32 (2014).
69. Wallace, D. P. Cyclic AMP-mediated cyst expansion. *Bba-Mol. Basis Dis.* **1812**, 1291–1300 (2011).
70. Yamaguchi, T. et al. Calcium restriction allows cAMP activation of the B-Raf/ERK pathway, switching cells to a cAMP-dependent growth-stimulated phenotype. *J. Biol. Chem.* **279**, 40419–40430 (2004).
71. Cabrera, I. et al. Cyst growth in ADPKD is prevented by pharmacological and genetic inhibition of TMEM16A in vivo. *Nat. Commun.* **11**, 4320 (2020).
72. Yang, B., Sonawane, N. D., Zhao, D., Somlo, S. & Verkman, A. Small-molecule CFTR inhibitors slow cyst growth in polycystic kidney disease. *J. Am. Soc. Nephrol.* **19**, 1300 (2008).
73. Digby, J. L. M., Vanichapol, T., Przepiorski, A., Davidson, A. J. & Sander, V. Evaluation of cisplatin-induced injury in human kidney organoids. *Am. J. Physiol. Ren. Physiol.* **318**, F971–F978 (2020).
74. Vaidya, V. S. et al. Kidney injury molecule-1 outperforms traditional biomarkers of kidney injury in preclinical biomarker qualification studies. *Nat. Biotechnol.* **28**, 478–485 (2010).
75. Han, W. K., Bailly, V., Abichandani, R., Thadhani, R. & Bonventre, J. V. Kidney Injury Molecule-1 (KIM-1): a novel biomarker for human renal proximal tubule injury. *Kidney Int* **62**, 237–244 (2002).
76. Ban, K. Y., Nam, G. Y., Kim, D., Oh, Y. S. & Jun, H. S. Prevention of LPS-induced acute kidney injury in mice by bavachin and its potential mechanisms. *Antioxidants (Basel)* **11**, 2096 (2022).
77. Zhang, W. et al. Kidney organoids as a novel platform to evaluate lipopolysaccharide-induced oxidative stress and apoptosis in acute kidney injury. *Front Med (Lausanne)* **8**, 766073 (2021).
78. Park, S. E. et al. Geometric engineering of organoid culture for enhanced organogenesis in a dish. *Nat. Methods* **19**, 1449 (2022).
79. Hiratsuka, K. et al. Organoid-on-a-chip model of human ARPKD reveals mechanosensing pathomechanisms for drug discovery. *Sci. Adv.* **8**, eabq0866 (2022).
80. Cho, A. N. et al. Microfluidic device with brain extracellular matrix promotes structural and functional maturation of human brain organoids. *Nat. Commun.* **12**, 4730 (2021).
81. Shin, W. et al. Spatiotemporal gradient and instability of wnt induce heterogeneous growth and differentiation of human intestinal organoids. *Iscience* **23**, 101372 (2020).
82. Neal, C. R. Podocytes... what's under yours?(podocytes and foot processes and how they change in nephropathy). *Front. Endocrinol.* **6**, 9 (2015).
83. Garg, P. A review of podocyte biology. *Am. J. Nephrol.* **47**, 3–13 (2018).
84. Ichimura, K. et al. Three-dimensional architecture of podocytes revealed by block-face scanning electron microscopy. *Sci. Rep. -Uk* **5**, 8993 (2015).
85. Fujigaki, Y. et al. Structural continuity of filtration slit (slit diaphragm) to plasma membrane of podocyte. *Kidney Int* **50**, 54–62 (1996).
86. Grahmmer, F., Schell, C. & Huber, T. B. The podocyte slit diaphragm—from a thin grey line to a complex signalling hub. *Nat. Rev. Nephrol.* **9**, 587–598 (2013).
87. Garreta, E. et al. Fine tuning the extracellular environment accelerates the derivation of kidney organoids from human pluripotent stem cells. *Nat. Mater.* **18**, 397–405 (2019).
88. Lawlor, K. T. et al. Cellular extrusion bioprinting improves kidney organoid reproducibility and conformation. *Nat. Mater.* **20**, 260–271 (2021).
89. Cruz, N. M. et al. Organoid cystogenesis reveals a critical role of microenvironment in human polycystic kidney disease. *Nat. Mater.* **16**, 1112–1119 (2017).
90. Cruz, N. M. et al. Modelling ciliopathy phenotypes in human tissues derived from pluripotent stem cells with genetically ablated cilia. *Nat. Biomed. Eng.* **6**, 463–475 (2022).
91. Bai, L. et al. AI-enabled organoids: construction, analysis, and application. *Bioact. Mater.* **31**, 525–548 (2024).
92. Liu, Y. et al. Prostaglandin E2 mediates proliferation and chloride secretion in ADPKD cystic renal epithelia. *Am. J. Physiol. -Ren. Physiol.* **303**, F1425–F1434 (2012).
93. Zafrani, L. & Ince, C. Microcirculation in acute and chronic kidney diseases. *Am. J. Kidney Dis.* **66**, 1083–1094 (2015).
94. Co, J. Y., Klein, J. A., Kang, S. & Homan, K. A. Suspended hydrogel culture as a method to scale up intestinal organoids. *Sci. Rep.* **13**, 10412 (2023).
95. Feng, Y. et al. Protocol for generating in vitro glioma models using human-induced pluripotent- or embryonic-stem-cell-derived cerebral organoids. *STAR Protoc.* **4**, 102346 (2023).
96. Sartore, R. C. et al. Trace elements during primordial plexiform network formation in human cerebral organoids. *PeerJ* **5**, e2927 (2017).
97. Sarrafha, L. et al. High-throughput generation of midbrain dopaminergic neuron organoids from reporter human pluripotent stem cells. *STAR Protoc.* **2**, 100463 (2021).
98. Przepiorski, A. et al. A simple bioreactor-based method to generate kidney organoids from pluripotent stem cells. *Stem Cell Rep.* **11**, 470–484 (2018).
99. Volmert, B. et al. A patterned human primitive heart organoid model generated by pluripotent stem cell self-organization. *Nat. Commun.* **14**, 8245 (2023).

100. Lewis-Israeli, Y. R. et al. Self-assembling human heart organoids for the modeling of cardiac development and congenital heart disease. *Nat. Commun.* **12**, 5142 (2021).
101. Renner, H. et al. Cell-type-specific high throughput toxicity testing in human midbrain organoids. *Front Mol. Neurosci.* **14**, 715054 (2021).
102. Katt, M. E., Placone, A. L., Wong, A. D., Xu, Z. N. S. & Searson, P. C. Tumor models: advantages, disadvantages, variables, and selecting the right platform. *Front Bioeng. Biotech.* **4**, 12 (2016).
103. Kim, W., Gwon, Y., Park, S., Kim, H. & Kim, J. Therapeutic strategies of three-dimensional stem cell spheroids and organoids for tissue repair and regeneration. *Bioact. Mater.* **19**, 50–74 (2023).
104. Yee, C., Dickson, K. A., Muntasir, M. N., Ma, Y. & Marsh, D. J. Three-dimensional modelling of ovarian cancer: from cell lines to organoids for discovery and personalized medicine. *Front Bioeng. Biotech.* **10**, 836984 (2022).
105. Kim, D., Youn, J., Lee, J., Kim, H. & Kim, D. S. Recent progress in fabrication of electrospun nanofiber membranes for developing physiological in vitro organ/tissue models. *Macromol. Biosci.* **23**, e2300244 (2023).
106. Ma, B. et al. Permeability of rhynchophylline across human intestinal cell in vitro. *Int J. Clin. Exp. Pathol.* **7**, 1957–1966 (2014).
107. Dekkers, J. F. et al. High-resolution 3D imaging of fixed and cleared organoids. *Nat. Protoc.* **14**, 1756–1771 (2019).
108. Stuart, T. et al. Comprehensive integration of single-cell data. *Cell* **177**, 1888 (2019).
109. Huang, D. W. et al. DAVID Bioinformatics resources: expanded annotation database and novel algorithms to better extract biology from large gene lists. *Nucleic Acids Res.* **35**, W169–W175 (2007).

Acknowledgements

This research was supported by the National Research Foundation (NRF) grant funded by the Korean government (MSIT) (NRF-2019M3A9H110 3769 and RS-2023-00208702, both received by D.S.K., and NRF-2022M3A9H1015716 and NRF-2020R1C1C1014753, both received by T.-E.P.) and by the Alchemist Project funded by the Ministry of Trade, Industry and Energy (MOTIE, Korea) (20012378, Development of Meta Soft Organ Module Manufacturing Technology without Immunity Rejection and Module Assembly Robot System, received by D.S.K.).

Author contributions

D.K. designed the research, performed the experiments, analyzed the data, and wrote the manuscript. H.L. performed the experiments,

analyzed the data, and wrote the manuscript. J.Y. provided assistance in the experiments and the preparation of the manuscript. T.E.P. supervised the research and wrote the manuscript. D.S.K. designed and supervised the research and wrote the manuscript.

Competing interests

The authors declare no competing financial interests.

Additional information

Supplementary information The online version contains supplementary material available at <https://doi.org/10.1038/s41467-024-53073-z>.

Correspondence and requests for materials should be addressed to Tae-Eun Park or Dong Sung Kim.

Peer review information *Nature Communications* thanks the anonymous reviewers for their contribution to the peer review of this work. A peer review file is available.

Reprints and permissions information is available at <http://www.nature.com/reprints>

Publisher's note Springer Nature remains neutral with regard to jurisdictional claims in published maps and institutional affiliations.

Open Access This article is licensed under a Creative Commons Attribution-NonCommercial-NoDerivatives 4.0 International License, which permits any non-commercial use, sharing, distribution and reproduction in any medium or format, as long as you give appropriate credit to the original author(s) and the source, provide a link to the Creative Commons licence, and indicate if you modified the licensed material. You do not have permission under this licence to share adapted material derived from this article or parts of it. The images or other third party material in this article are included in the article's Creative Commons licence, unless indicated otherwise in a credit line to the material. If material is not included in the article's Creative Commons licence and your intended use is not permitted by statutory regulation or exceeds the permitted use, you will need to obtain permission directly from the copyright holder. To view a copy of this licence, visit <http://creativecommons.org/licenses/by-nc-nd/4.0/>.

© The Author(s) 2024